Polyglutamic acid-based Crosslinked Doxorubicin Nanogels as an Anti-Metastatic Treatment for Triple Negative Breast Cancer

Aroa Duro-Castano[†I], Ana Sousa-Herves[‡I], Ana Armiñán[†], David Charbonnier[†], Juan José Arroyo-Crespo[†], Stefanie Wedepohl[‡], Marcelo Calderón[§,⊥], María J. Vicent[†*]*

[†]Polymer Therapeutics Lab, Centro de Investigación Príncipe Felipe, Eduardo Primo Yúfera 3, 46012 Valencia, Spain

[‡]Freie Universität Berlin, Institut für Chemie und Biochemie, Takustrasse 3, 14195 Berlin, Germany

[§]POLYMAT & Applied Chemistry Department, Faculty of Chemistry, University of the Basque Country UPV/EHU, Paseo Manuel de Lardizabal 3, 20018, Donostia-San Sebastián, Spain

[⊥]IKERBASQUE, Basque Foundation for Science, 48013 Bilbao, Spain

*Co-corresponding Authors
María J. Vicent mjvicent@cipf.es; Marcelo Calderón marcelo.calderon@polymat.eu
[I]Authors with equal contribution

Present Addresses

Aroa Duro-Castano. Department of Chemistry, University College London (UCL), 20 Gordon Street, London, WC1H 0AJ, United Kingdom

Ana Sousa-Herves. Departamento de Química Inorgánica, Orgánica y Bioquímica, Facultad de Farmacia, Universidad de Castilla-La Mancha, C/José María Sánchez Ibañez s/n, 02071, Albacete, Spain.

Keywords

Polypeptides, Polyglutamic Acid, Nanogel, Drug Delivery, Triple Negative Breast Cancer, Lung Metastases, Lymph node Metastases

Abstract

Treatment of triple negative breast cancer (TNBC)-associated metastasis represents an unmet clinical need, and we lack effective therapeutics for a disease that exhibits high relapse rates and associates with poor patient outcomes. Advanced nanosized drug delivery systems may enhance the efficacy of first-line chemotherapeutics by altering drug pharmacokinetics and enhancing tumor/metastasis targeting to significantly improve efficacy and safety. Herein, we propose the application of injectable poly-amino acid-based nanogels (NGs) as a versatile hydrophilic drug delivery platform for the treatment of TNBC lung metastasis. We prepared biocompatible and biodegradable cross-linked NGs from polyglutamic acid (PGA) loaded with the chemotherapeutic agent doxorubicin (DOX). Our optimized synthetic procedures generated NGs of ~100 nm in size and 25 wt% drug loading content that became rapidly internalized in TNBC cell lines and displayed IC50 values comparable to the free form of DOX. Importantly, PGA-DOX NGs significantly inhibited lung metastases and almost completely suppressed lymph node metastases in a spontaneously metastatic orthotopic mouse TNBC model. Overall, our newly developed PGA-DOX NGs represent a potentially effective therapeutic strategy for the treatment of TNBC metastases.

1. Introduction

Nanogels (NGs, nanometer-sized gels) have drawn significant recent attention as pharmaceutical nanocarriers as they possess advantageous characteristics of both hydrogels and nanoparticles.[1-3] NGs represent a versatile hydrophilic drug delivery platform for the controlled site-specific release of hydrophobic drugs and biomacromolecules such as proteins or nucleic acids.[4] Due to their inherent porosity, NGs also offer unusually high drug loading capacities compared to liposomes or polymeric micelles and can incorporate greater than 30% wt of a given cargo. Furthermore, the swelling properties of NGs allow for controlled cargo release in response to several environmental stimuli (e.g., ionic strength, pH, or temperature).[5-7] In this sense, NGs that display stimuli-responsive cargo release in the tumor microenvironment are especially appealing.[8-10]

The physico-chemical properties of the three-dimensional cross-linked nanoscale polymer network of NGs, such as size, charge, porosity, softness, amphiphilic character, and degradability, can be varied by chemical composition (polymer and cross-linking agents) to allow a range of potential biological applications; however, few NGs have reached clinical trials, and NGs have yet to meet approval. This unfortunate circumstance partly derives from the low mechanical and biological stability of NGs under physiological conditions based on physical interactions.[11] Nevertheless, chemically cross-linked NGs have the potential to overcome said limitations and become more widely applied, even in intravenous administrations.[11] In this context, cross-linked polypeptides and poly-amino acid (PAA)-based NGs can surpass many of the problems associated with other NGs, including those related to solubility, scalability, reproducibility, biodegradability, administration, and long-term accumulation.

Biodegradable and biocompatible PAA-based polymers[12] can be synthesized in a scalable and reproducible manner by controlled polymerization techniques, and an ever-increasing number of examples reaching preclinical and clinical stages has highlighted their relevance to drug delivery.[12] Of particular interest, poly-*L*-glutamic acid (PGA) represent a promising candidate, with a PGA-paclitaxel conjugate (Opaxio®) and several other anticancer PGA-based micelles currently in advanced clinical trials.[13]

The use of PAAs in the preparation of NGs has been limited to the formation of electrostatic complexes with polycationic entities,[14,15] or the cross-linking of a polymeric micelle core composed of polyethylene glycol (PEG)-PAA block copolymers.[16-18] Furthermore, the implementation of PAAs in NGs for the treatment of metastasis has yet to be explored in any great depth[19] with no examples of a breast cancer-associated metastasis targeted PAA-based NG therapeutic.

The triple negative breast cancer subtype (TNBC, lacks estrogen receptors, progesterone receptors, and HER2 expression) represents about 10-20% of all breast cancer diagnoses. The aggressive characteristics of TNBC include metastasis to regional lymph nodes and distant organs and high relapse rates, which combine to foster an overall poorer prognosis when compared with other subtypes.[20] Lung metastasis represents a recurrent complication, occurring in 60-70% of all breast cancer patients, and a leading cause of patient deaths.[21] Meanwhile, the metastatic load of lymph nodes represents an important prognostic factor and frequently decides therapy choice.[22,23]

Herein, we describe the first example of anionic chemically-crosslinked NGs exclusively formed from the biodegradable and biocompatible PGA polymer. We employed copper-catalyzed azide-alkyne cycloaddition (CuAAC)[24] to prepare cross-linked PGA NGs in inverse miniemulsion, thus allowing control over size and dispersity (Scheme 1). Importantly, we designed PGA NGs to become rapidly degraded in the presence of Cathepsin B, a lysosomal enzyme that also is overexpressed in the stroma of certain types of tumors, to promote tumor-specific drug release (bioresponsiveness). Following loading with the chemotherapy agent doxorubicin (DOX), we explored the potential for our bioresponsive PGA-DOX NG-based strategy to treat TNBC-associated lung and lymph node metastases in a murine model. Encouragingly, we discovered that PGA-DOX NGs exert antitumor activity *in vivo* and, more importantly, a significant antimetastatic effect with a near-complete reduction in metastasis.
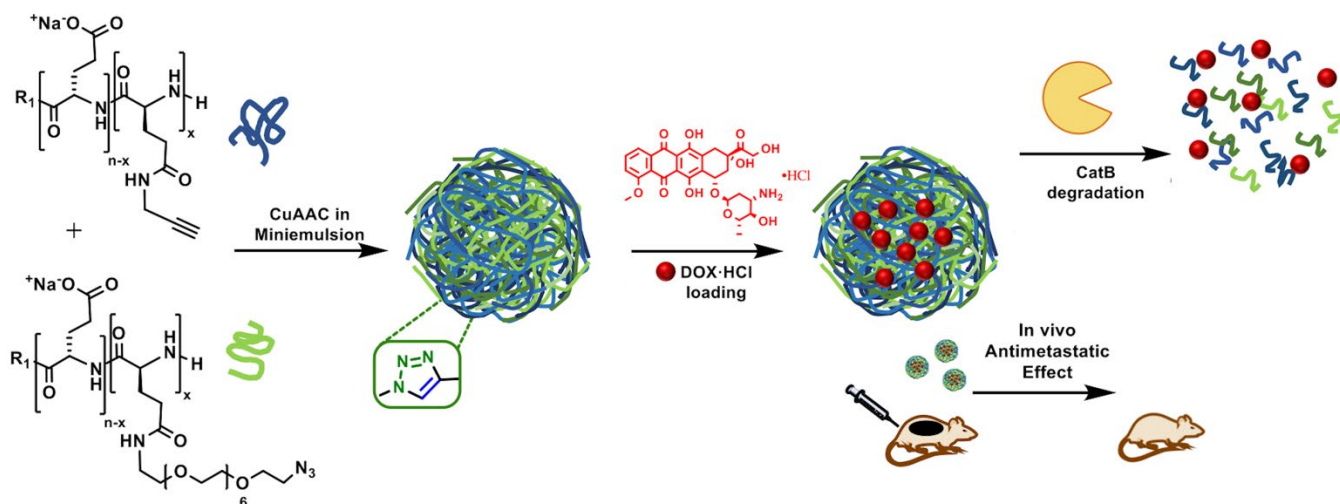
Scheme 1. Synthesis and mode of action of bioresponsive cross-linked PGA-DOX NGs

2. Materials and Methods

Materials

All chemicals, cells, animals, and materials used in this study are fully described in the Electronic Supporting Information (ESI).

Physicochemical Characterization

Information regarding NMR spectroscopy, circular dichroism (CD), dynamic light scattering (DLS), z-potential analysis, Fourier-transform infrared spectroscopy (FT-IR), ultraviolet-visible (UV-Vis) spectroscopy, scanning electron microscopy (SEM), atomic force microscopy (AFM), and cryo-transmission electron microscopy (Cryo-TEM) measurements and experimental conditions can be found in the ESI.

Synthesis of Alkyne- and Azide-derivatized PGA Precursors

PGA precursors were synthesized according to Barz et al.[25] and provided yields of 80-90% and conjugation efficiencies of 90-100%. The ESI contains the chemical structures (Scheme S1) as well as additional details.

Optimization of PGA-PGA Coupling Conditions by CuAAC

Several reaction parameters were evaluated to explore the most suitable CuAAC conditions for the coupling of PGA-azide and PGA-alkyne precursors. More specifically, polymers **1** and **3** (Table S1) were selected, and CuAAC coupling was performed in H_2O. A representative example (see Entry 4 in Table 1) is described as follows: 3 mg of PGA-N_3 (10% functionalization, compound **1**, 1.65 μmol of N_3 groups), 7.5 mg of PGA-Alkyne (10% functionalization, compound **3**, 4.95 μmol of Alkyne groups), and 6.09 mg of $NaHCO_3$ (1.1 eq of per COOH group) were dissolved in an aqueous solution of $CuSO_4$ (0.05 M, 66 μL). After stirring, 165 μL of a 0.1 M sodium ascorbate solution was added. The mixture was allowed to react at 40 ºC for 48 h protected from light. The crude product was then purified using Amicon centrifugal filters, and then lyophilized and analyzed by ^1H NMR and IR spectroscopies.

Preparation of PGA-based NGs by CuAAC Crosslinking in Miniemulsion

NGs were synthesized by CuAAC cross-linking using a miniemulsion technique to template NG formation. In a representative example, PGA-co-EG(n)N_3 glutamate 10% (**1** in Scheme S1, 21 mg, 1 eq of N_3 groups, 11.5 μmol), PGA-co-propargyl glutamate (**3** in Scheme S1, 34.8 mg, 2 eq of alkyne groups, 23 μmol), and $NaHCO_3$ (23.6 mg, 1.1 eq per carboxylic acid group) were dissolved in 340 μL of MilliQ water. Freshly prepared aqueous solutions of $CuSO_4$ (46 μL, 0.2 eq per N_3) and sodium ascorbate (115 μL, 1 eq per N_3) were added. Immediately afterward, the aqueous solution was mixed with 15 mL of cyclohexane containing Tween® 80 (100 mg) and Span® 80 (300 mg). The mixture was then ultrasonicated with a Branson Digital Sonifier (2 × 2 min at 50% intensity), yielding a stable emulsion. DLS measurements were performed following ultrasonication to check nanodroplet size and dispersity. The resulting emulsion was stirred at 40 °C for 48 h, and then 15 mL of cyclohexane was added, and the solution was centrifuged (30 min, 6000 rpm). A gel-like precipitate was observed; the supernatant was then removed, and fresh cyclohexane was added. This procedure was repeated three times to remove surfactants. After complete solvent drying, MilliQ water was added, and the resulting solution was dialyzed (MWCO 50 KDa) or washed extensively using Amicon centrifugal filters (MWCO 50 KDa). To ensure copper removal[26] (see ESI, section 3), NGs were sequentially washed with a solution of HCl pH 3

6

(2 ×), NaHCO$_3$ (2 ×), and Milli Q water (4 ×). The resulting NGs (31 mg) were analyzed by DLS (2 mg/mL in H2O, filtered by 0.45 μm nylon filters), AFM, SEM, cryo-TEM, IR, and ^{1}H NMR. Finally, the resulting NGs were freeze-dried or stored in solution at 4 °C.

General Procedures for the Preparation of PGA-DOX NGs

DOX·HCl was dissolved at 3 mg/mL in a mixture of 10 mM NaH$_2$PO$_4$, 1 M HCl, and DMSO (100:1:5.5). PGA NGs were separately dissolved at 2.5 mg/mL in 10 mM Na$_2$HPO$_4$, 1 M NaOH (100:1). Both solutions were mixed (0.75 mg DOX per mg of NG), and pH measured, adjusted to pH 7 if necessary, and stirred overnight protected from the light. PGA-DOX NGs were purified by extensively washing using Amicon Ultra-15 centrifugal filters (MWCO 50 KDa) until no red solution was observed, and subsequently freeze-dried. After purification, NGs were run through a Sephadex G25 column (1 mL) to verify the absence of free DOX. The amount of encapsulated DOX was estimated by UV-Vis spectroscopy in H$_2$O (λ = 488 nm, ε = 11,500 L mol^{-1} cm^{-1}, ESI). Mass recoveries varied between 10 and 30%.

Drug Release and Plasma Stability

Drug release profiles were analyzed following a previously described procedure.[27] Briefly, 2 mg of NGs were weighed and separately dissolved in 20 mM acetate buffer pH 6 containing EDTA, Dithiothreitol (DTT), and Cathepsin B (final concentration 4.16 units/mL), PBS pH 5.5 (10 mM, 150 mM NaCl), PBS pH 7.4 (10 mM, 150 mM NaCl, Figure S6) or mouse plasma. DTT and EDTA solutions were added as optimal Cathepsin B activity requires pH < 6 and a reductive environment. NGs were placed in a bath at 37 ºC with magnetic stirring. At specified time intervals, aliquots were taken and run through a small (0.9 mL) Sephadex G25 column in MilliQ water. Free DOX was retained in the upper part of the column, while NGs could be collected, freeze-dried, dissolved in Milli Q water, and analyzed by UV-Vis to determine DOX levels (λ = 488 nm, ε = 11500 L mol^{-1} cm^{-1}). Data represent the mean ± SEM of three measurements.

Biological Procedures

All biological procedures employed in this study are fully described in the ESI, including cell culture protocols, MTS assays for cell viability, cellular uptake by flow cytometry, confocal fluorescence microscopy, Annexin V by flow cytometry, cell cycle by flow cytometry, tumor model, determination of metastases, and Western blot analyses.

3. Results and Discussion

Preparation of Injectable PGA NGs with suitable Physico-chemical Properties

For the development of PGA NGs, we synthesized a series of alkyne- and azide-derivatized PGAs as a first step (as previously described by us in Barz et al.[25]) using a PGA with a molecular weight (Mw) of 10,500 Da and polydispersity (PDI) of 1.1.[28] We employed propargylamine and oligoethylene glycol azide residues for alkyne and azide functionalization, respectively, to yield compounds with orthogonal functionalities (see Scheme 1, Scheme S1, and Table S1 in the ESI).

CuAAC is a simple and powerful coupling technology for the conjugation of polymers and other macromolecules; nevertheless, the presence of Cu traces represents a potential concern. Therefore, we optimized the CuAAC coupling conditions in aqueous solution before the preparation of NGs to yield enhanced cross-linking efficiency while using the minimum amount of catalyst. Moreover, we established efficient protocols to remove trace Cu, as demonstrated by MTT assays (Section 3c, ESI).

We evaluated several reaction conditions to define those steps required for efficient PGA-azide/PGA-alkyne coupling for the different PGA precursors (Table 1). More specifically, we selected polymers **1** and **3** (Table S1) and performed CuAAC coupling in H_2O, employing 1.1 eq of $NaHCO_3$ per COOH group.[26] We fixed the reaction time at 48 h and performed a set of reactions changing the reaction temperature, the amount of copper catalyst, and the ratio between azide and alkyne functional groups. The optimal reaction conditions are described in entry 4 of Table 1. Initially, we used an excess of alkyne

groups to facilitate reaction monitoring by following the disappearance of the signal at *ca.* 3.4 ppm (characteristic of the methylene protons adjacent to the azide groups) in the ^{1}H NMR spectra, as well as by the appearance of the triazole peak at *ca.* 8.0 ppm (Figure 1a).

Moreover, we employed IR spectroscopy to monitor the disappearance of the intense characteristic azide signal at 2100 cm^{-1} (Figure 1b). Following the optimization of the CuAAC conditions, we assessed a series of PGA precursors (compounds **1-5**, Table S1) that displayed different degrees of functionalization (10%, 17% for both azide and alkyne building blocks, compounds **1-4** in Table S1) and then evaluated the effect of short PEG linkers of different lengths (6 and 2 units, compounds **1** and **2** *vs.* **5** in Table S1). We hypothesized that both parameters could affect coupling efficiency through the CuAAC reaction; however, we obtained PGA-PGA copolymers in all cases (Entries **6-8** in Table 1).

Table 1. PGA precursors and CuAAC conditions assessed

Entry	Alkyne/N$_3$ molar ratio	% Alkyne/ N$_3$[a]	Equivalents CuSO$_4$/Na Ascorbate[b]	T (ºC)
1	2/1	10/10	0.05/0.25	rt
2	1/2	10/10	0.05/0.25	rt
3	1/2	10/10	0.20/1	rt
4	3/1	10/10	0.20/1	40
5	1/2	10/10	0.20/1	40
6	3/1	17/17	0.20/1	40
7	3/1	10/18	0.20/1	40
8	3/1	17/10	0.20/1	40

[a]Degree of functionalization of PGA polymers (compounds **1-5** in Table S1). [b]Equivalents calculated per N$_3$ group

In the next step, we screened several PGA precursors with different degrees of functionalization to synthesize NGs suitable for biological applications, i.e., with adequate size, stability, and low PDI. Furthermore, we wanted to explore the effect of a higher cross-linking degree on NG size, stability, and swelling behavior. Table 2 summarizes all the PGA NGs prepared.

We obtained NGs by CuAAC cross-linking using inverse miniemulsion, a technique that allows the creation of stable nanodroplets in a continuous phase by applying high shear stress, such as those associated with ultrasonication. Subsequently, the cross-linking takes place inside the nanodroplets, and we finally obtained NGs after extensive purification in cyclohexane and MilliQ water.

DLS analysis demonstrated that combinations of polymers with similar functionalization degrees resulted in NGs with lower PDI values. PGA precursors with 10 % functionalization (NG 1 in Table 2, prepared from compounds 1 and 3 in Table S1) represented one of the most promising combinations in terms of PDI and reproducibility. We hypothesized that a lower degree of cross-linking within the polymeric network of the NG might provide a more flexible polymeric nanostructure, and, therefore, an enhanced capability to physically encapsulate and release hydrophobic drugs.[29,30] For these reasons, we chose PGA NG 1 for DOX loading.

Finally, ^{1}H NMR and FT-IR spectroscopies (Figures S1 and S2, ESI) confirmed the complete chemical coupling for PGA NG 1 by highlighting the appearance of the triazole peak and the disappearance of the characteristic azide stretching band, respectively.

Table 2. Summary of the PGA-based NGs screened

NG	%Alkyne/ Azide	PGA Alkyne/ Azide Precursors[a]	Dh (nm)[b]	PDI[b]
NG 1	10/10	3 and 1	108	0.13
NG 2	17/17	4 and 2	130	0.22
NG 3	17/18	4 and 5	134	0.21
NG 4	17/10	4 and 1	n.d.	0.48

[a]From Table S1. [b]Determined by DLS (mean intensity). n.d. Not determined due to multimodal distribution. Dh: hydrodynamic diameter. PDI: polydispersity.
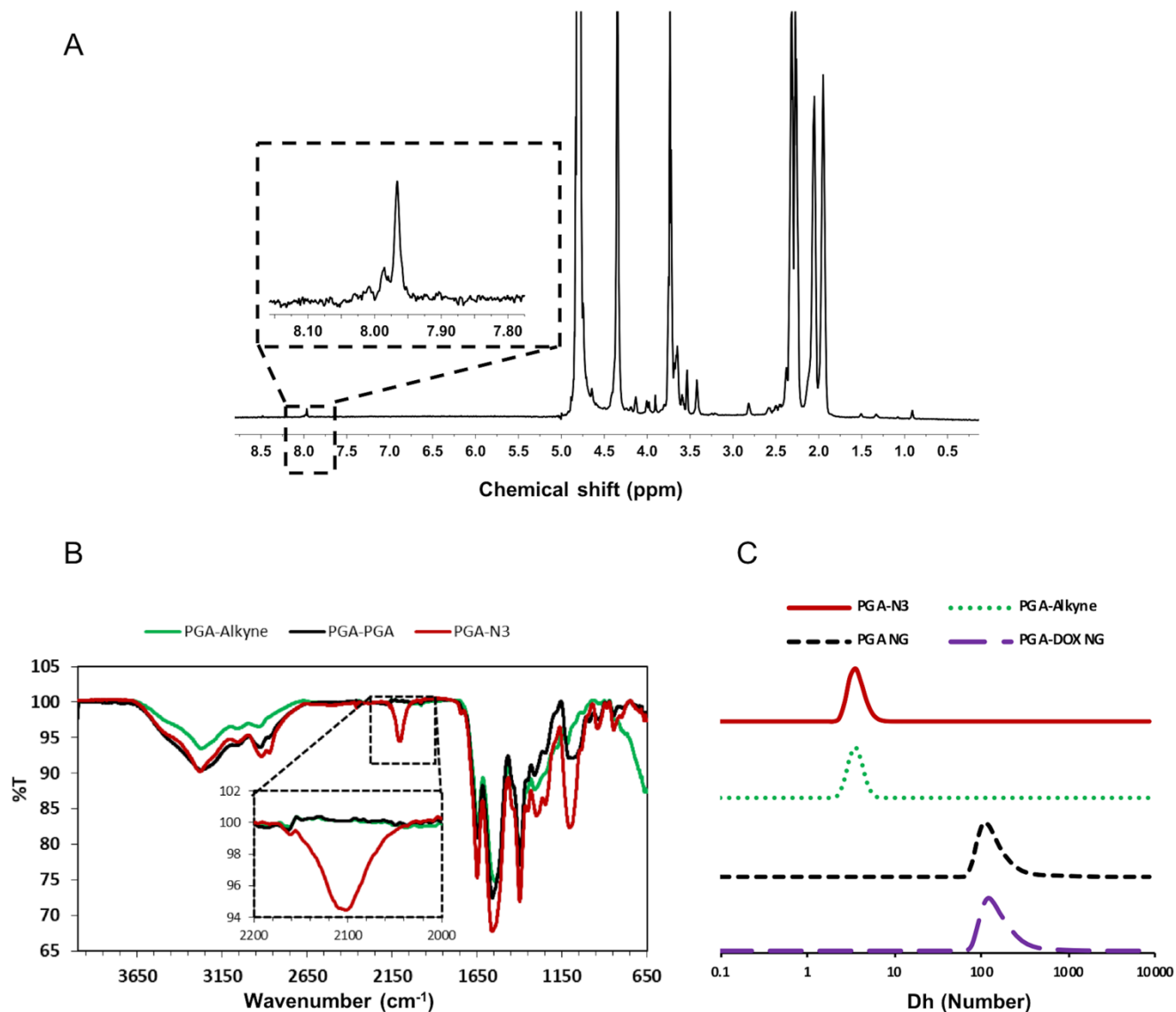
Figure 1. A. Representative ^{1}H NMR spectra (D_2O) of CuAAC coupling of PGA polymers, demonstrating the presence of the triazole peak. **B**. FT-IR-spectra of CuAAC cross-linking after coupling (black) compared to PGA-N_3 (red). **C**. Hydrodynamic diameter (Dh) analysis in MilliQ H_2O represented in number reveals small particle sizes of ~4 nm for PGA copolymers (PGA-N_3 and PGA-Alkyne, Table S1 compounds **1** and **3** respectively) whereas particle sizes larger than 100 nm were found for PGA NG and PGA-DOX NG.

Efficient DOX loading into PGA NGs

We employed DOX as a model chemotherapeutic drug, given that it represents one of the current standards of care for metastatic breast cancer. We encapsulated DOX after PGA NG formation via a simple

method based on electrostatic interactions between cationic DOX and the carboxylic acid groups of PGA.[31] We estimated drug loading content (DLC) and drug loading efficiency (DLE) of DOX by UV-VIS measurements at λ= 488 nm (Figure S4) and calculated values according to Equations S1 and S2 (ESI). The typical DLC and DLE values (wt%) averaged at around 25 and 33, respectively, which agrees well with other studies reporting DOX entrapment by electrostatic interactions.[32,33]

PGA NGs exhibited particle sizes of 225 nm with a PDI < 0.29 and good batch-to-batch reproducibility (in terms of size and PDI) as determined by DLS. Notably, we observed an increase in the negative z-potential measured for PGA-copolymers (~-20 mV) when they formed PGA NGs (~-49 mV), as previously observed with other PGA nanoparticles with a particle size around 100 nm.[34] PGA-DOX NGs displayed a less negative z-potential (~-18 mV) due to the encapsulation of the positively charged DOX. Circular dichroism spectra of empty and loaded nanogels can be found in (Figure S5). In particular, the CD spectrum of PGA-DOX NGs shows the typical peaks of the DOX chromophore with its set of $\pi \rightarrow$ π^* and n $\rightarrow$ π^* transitions, and the characteristic negative band at 540 nm for DOX dimerization.[35]
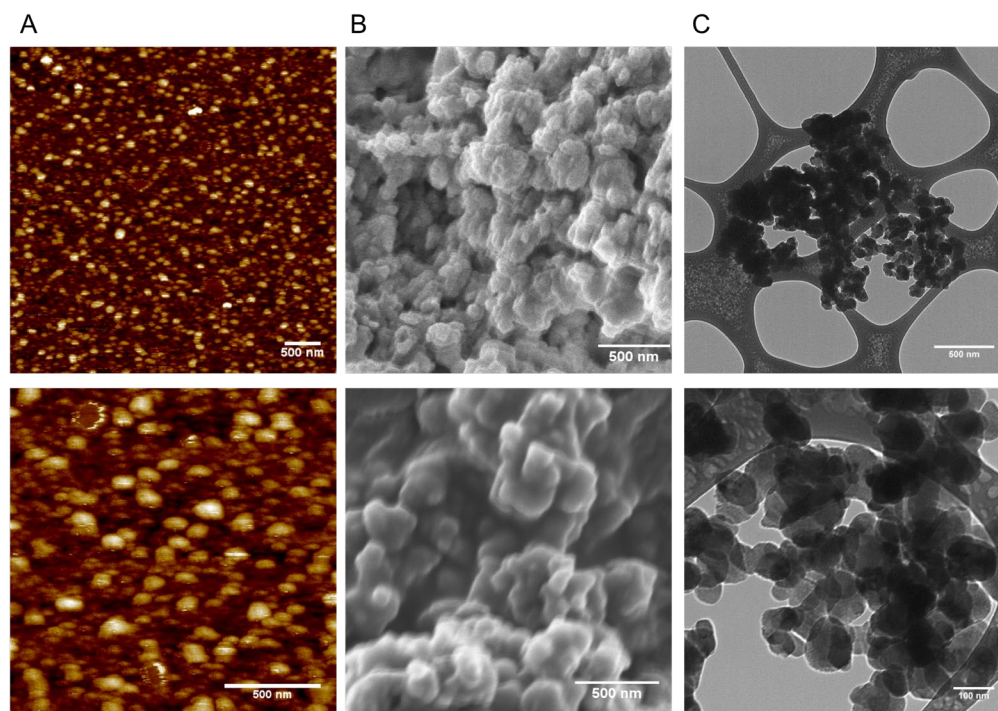

Figure 2. Morphology of cross-linked PGA NGs using various microscopic techniques. **A)** AFM images of cross-linked PGA NGs at different resolutions (1700 x 1700 nm lower image, and 4500 x 4500 nm

upper image). Scale-bar 500 nm in both upper and lower images. **B**). SEM images of cross-linked PGA NGs. Scale bars 500 nm. **C**) Cryo-TEM images of cross-linked PGA-DOX NGs at 0.1 mg/mL in MilliQ H_2O. Scale bars 500 nm in the upper image and 100 nm in the lower magnification image.

We next assessed the size, surface topology, and morphology of PGA and PGA-DOX NGs through various microscopy techniques, with the results mostly consistent with the data previously obtained by DLS. Cryo-TEM, SEM, and AFM micrographs of PGA NGs/PGA-DOX NGs revealed a spherical shape of the nanoparticles. Statistical analysis of AFM images showed a mean diameter of 98.2 ± 30 nm. Cryo-TEM, SEM, and AFM micrographs of PGA NGs/PGA-DOX NGs revealed a spherical shape of the nanoparticles (Figure 2).

PGA-DOX NGs display Cathepsin B-triggered Drug Release and Efficient Internalization in TNBC Cells.

Depending on the rational design strategy employed, multiple mechanisms mediate drug release from NGs. These include simple diffusion, degradation of NG structure, pH and temperature changes, counterion displacement or an external trigger[4]. PGA is a well-known biodegradable and biocompatible polypeptide, mainly degraded by cysteine proteases such as the lysosomal Cathepsin B.[36,37] The degradation of PGA by lysosomal enzymes has been extensively studied *in vitro* although less extensively *in vivo.*[38] In the design of our bioresponsive PGA-DOX NGs, the enzymatic degradation of the polymeric chain will trigger drug release at the desired site of action (tumor microenvironment and within tumor cells), thereby enhancing therapeutic efficiency and reducing unwanted side effects. Although other proteases may play a role in the enzymatic degradation of PGA backbones, Cathepsin B has been identified as the major actor by Shaffer et al.[36] Thus, drug release studies in the presence of Cathepsin B could

provide an estimate of the *in vivo* biological performance of our constructs. Furthermore, we have previously demonstrated the Cathepsin B-dependent biodegradability of star-shaped and linear PGA polymers.[27]

Figure 3A establishes that degradation of the nanogel structure by Cathepsin B is the major drug release mechanism triggering a rapid release of DOX from NGs, with already 80% of drug release at 8 h post-treatment. This fact validates the suitability of these systems for lysosomotropic DOX delivery and/or for triggering drug release in the TNBC tumor microenvironment where cathepsin B is also overexpressed, in particular, in those tumors with the worst prognosis.[39,40] Release studies with the enzyme were performed at pH 6, as Cathepsin B is a lysosomal enzyme and requires acidic pH and reductive environment to be active.[27] Although in our experiments we reach a plateau at 80 % drug release, we envisage complete release in a more complex cellular environment, as PGA degradation will not only rely on cathepsin B but also in other proteases present. Another possible explanation of this incomplete release could derive from difficulties in DOX quantification in our experimental conditions due to a possible formation of a colloidal suspension of DOX upon release.

PGA-DOX NGs show minimum drug release when incubated in mouse plasma for 24 hours, an indication of adequate plasma stability for i.v. administration. This fact can be presumably explained by the formation of a plasma-derived protein corona. Previous works have also noted altered drug release from NGs as a result of the protein corona, suggesting potential differences in in vitro or in vivo release profiles.[41] The control drug release studies in buffer conditions show lower DOX release rate as compared to the one obtained with Cathepsin B. The similar release rates at pH 5.5 and 7.4 (Figure S6) could arise from the nanogel swelling and presence of the high ionic strength (150 mM) that may cause dissociation between the ionic complex DOX/COOH. pH responsiveness could be achieved if pH sensitive functional groups that deionize in the polymeric network are introduced, in this case pKa of PGA is around 5.5[34] therefore such pH responsiveness at physiological pHs were not observed (Figure S6). Only very acidic pH values (not relevant when i.v. administered compounds) would prompt a differential pH-induced release.
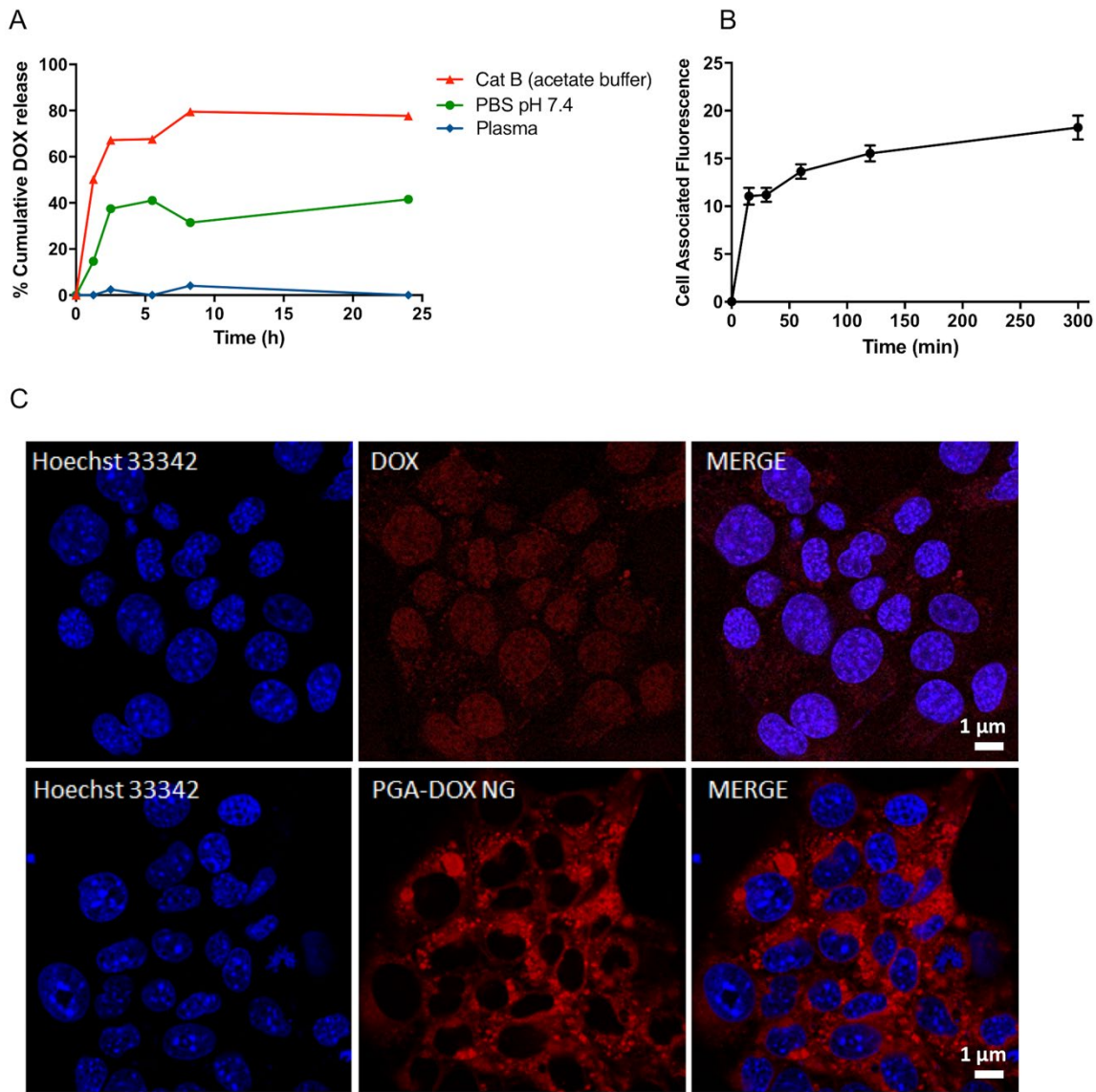
Figure 3. **A**. Drug release profile of PGA-DOX NG in the presence of Cathepsin B (Cat B, triangles) and under physiological pH control conditions (PBS pH 7.4, circles) and plasma (diamonds) demonstrate a non-significant release in plasma and a burst release under enzymatic or hydrolytic conditions with a maximum of drug release of 80 % with Cathepsin B (n=3, data as mean ± SEM). **B**. Cell-associated fluorescence over time of PGA-NG DOX at 37 °C in the 4T1 murine breast cancer cell line suggests cellular uptake, indicative of co-operative mechanisms of internalization (n > 3, mean ± SEM). **C**. Confocal images of DOX (upper) and PGA-DOX NG (lower) uptake at 15 min post-treatment in 4T1 cells following a pulse-chase experiment (Blue-Hoechst 33342 for nuclei; Red-DOX associated fluorescence). The localization of DOX to the nucleus, while PGA-DOX NGs were absent, suggests altered internalization kinetics.

Understanding the cellular internalization mechanisms employed by nanomedicines represents a mandatory step in the drug delivery field.[42] Linear and branched PGAs follow endocytic mechanisms of internalization, and so represent suitable candidates for lysosomotropic drug delivery.[27,34] Drug release from PGA-DOX NGs relies on the action of lysosomal endopeptidases, thereby requiring efficient cellular uptake following a lysosomotropic delivery route.

To investigate whether PGA-DOX NGs, whose physico-chemical features differ from conventional lineal PGA-drug conjugates, follow the same uptake mechanism, we performed live-cell *in vitro* studies. We employed flow cytometry (for the quantification of cell uptake) together with live-cell confocal microscopy analysis (for the qualitative visualization of subcellular fate and pathway) in the 4T1 murine breast cancer cells (TNBC and with high metastatic potential). We observed a high and rapid internalization rate (represented by the cell associated fluorescence, Figure 3B) for PGA-DOX NG in 4T1 cells at 37 °C. While we observed free DOX in the nucleus at 15 min at 37 °C (see Figure 3C, Figures S7, and S8), as expected for a DNA intercalator, we encountered PGA-DOX NGs co-localizing with the lysosomes at a later timepoint, at 1 h post-treatment (Figure 3C, Figure S9). These data suggest that PGA-DOX NGs exhibited a different internalization route and kinetics than the free form of DOX. Furthermore, confocal images suggested that PGA-DOX NGs allowed for increased drug uptake (when compared to free DOX). The fact that DOX encapsulated within our nanogels does not follow a diffusion mechanism of cell entry, but instead, an energy-dependent endocytic uptake mechanism and lysosomotropic trafficking, indicates that DOX delivered this way escapes the drug-efflux pumps, the ATP-binding cassette (ABC) transporters located in the cell membrane, and thus, would avoid a potential drug-resistance.[43-45] The final fate of DOX in due time would be the nucleus as per its topoisomerase II defined target.

PGA-DOX NGs exert *In-vitro* Antitumor Activity in TNBC Cells

We next assessed the cytotoxic effects of PGA-DOX NGs in 4T1 cells compared to free DOX and the control PGA NG, the later showing absence of cytotoxicity up to the concentration tested. Overall, PGA-DOX NGs exerted a similar cytotoxic activity when compared to free DOX, with IC50 values of

0.3102 and 0.1825 µg/mL eq. DOX, respectively (Figure 4A, Table S2). Apoptosis assays with Annexin V revealed a trend towards fewer apoptotic cells following treatment with PGA-DOX NGs compared to DOX during 72 h, although any differences failed to reach significance (Figure S10).
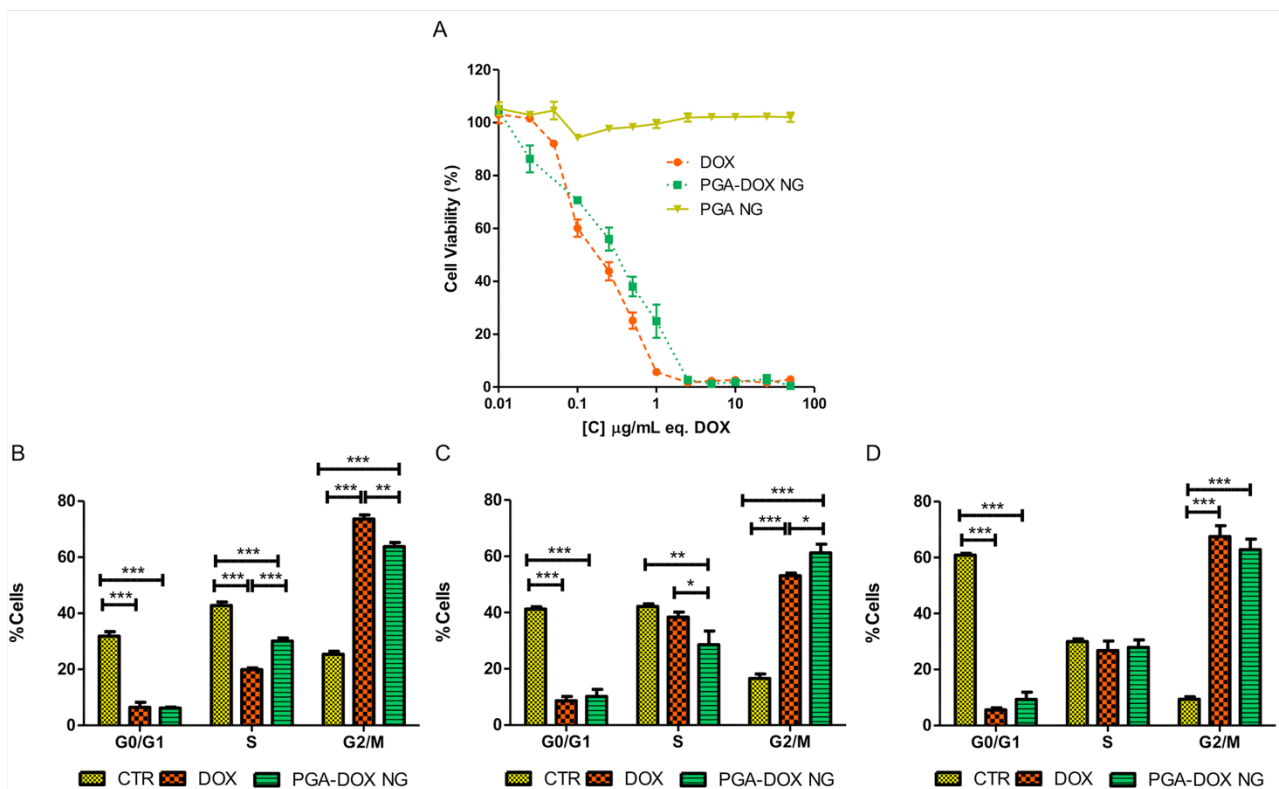

Figure 4. **A**. Cell viability curves for IC50 determination in 4T1 cells after 72 hours of treatment with PGA NGs/PGA-DOX NGs measured by MTS assay shows similar *in vitro* antitumor activity of PGA-DOX NG (green) when compared to free DOX (red). Unloaded PGA NGs evaluated at an equivalent polymer concentration of the PGA-DOX NG failed to exhibit toxicity at the concentrations evaluated (n>4 independent experiments with 6 replicates each, mean ± SEM). **B-D**. Cell cycle analysis using propidium iodide (PI) staining and flow cytometry. 4T1 cells were treated for 24 h (**B**), 48 h (**C**), and 72 h (**D**) at the IC50 values obtained by MTS assays (72 h). CTR: Control cells without treatment. Results are the mean ± SEM of three independent experiments with two replicates each. One-way ANOVA and Bonferroni post hoc were used for comparison between groups. *$P<0.05$; **$P<0.01$; ***$P<0.001$; ns: non-significant.

Cell cycle analysis using propidium iodide (PI) staining and flow cytometry demonstrated a similar pattern for both DOX and PGA-DOX NGs after 72 h of treatment (Figure 4D). Nevertheless, at earlier

time points (24 h and 48 h of treatment Figures 4B and C, respectively), we observed statistically significant differences between DOX and PGA-DOX NGs. These differences became "normalized" over time, suggesting different kinetics in the mechanism of action that could be closely related to the different kinetics found for the internalization rate and drug bioavailability. Cell cycle analysis revealed that, as a general trend, both DOX and PGA-DOX NGs promoted cell accumulation in the G2/M phase to the detriment of G0/G1 when compared to untreated control 4T1 cells. These facts suggest a cell cycle arrest, which hinders cell division and ultimately leads to cell death, a finding that agrees with previous reports regarding the mechanism of action of DOX *in vitro*.[46]

Injectable PGA-DOX NGs Prompt Significant Reductions in Primary Tumor Volume and Weight in a Mouse TNBC Model

Our *in vitro* data encouraged us to evaluate our PGA-DOX NGs in a spontaneously metastatic TNBC orthotopic murine model.[47] We inoculated animals in the mammary fat pad with 4T1 cells following previously optimized protocols.[48,49] Treatments began at day 8, a time point that coincided with the maximum enhanced permeability and retention effect[50] when tumors sizes had reached ~0.1 cm^3, to promote efficient tumor uptake. After intravenous injection through the tail vein (three doses every three days), we monitored tumor growth for 16 days. As additional controls, we employed free DOX and a PGA-DOX conjugate synthesized with a non-biodegradable linker that significant diminish DOX release in order to remark the importance of an adequate drug release profile as previously demonstrated.[48,49] We used free DOX doses of 3 mg/kg due to previously observed toxicity with higher DOX doses;[48,49] however, we could apply doses up to 10 mg/kg of DOX equivalents for PGA-DOX conjugate and PGA-DOX NGs without observed toxicity, which represents an advantage of the PGA formulations compared with free DOX treatment.

We systematically evaluated the general aspect, behavior, body weight (Figure 5A), and post-mortem major organ weights of all animals (Figure S11) to assess safety. Of note, we failed to observe significant animal weight or major organ weight alterations in response to any treatment (Figure 5A and Figure S11). At the experimental endpoint, PGA-DOX NGs significantly reduced the primary tumor volume (24% - see Figure 5B); however, we failed to observe any antitumoral effect for the control PGA-DOX conjugate, while free DOX treatment provided no statistically significant improvement over PBS treated controls (Figure 5B). The statistics included in Figure 5B imply non-significant differences between DOX and PGA-DOX NGs in this particular case. Moreover, only PGA-DOX NGs displayed statistically significant decreases in tumor weight compared to PBS and PGA-DOX conjugate treatment (Figure 5C).
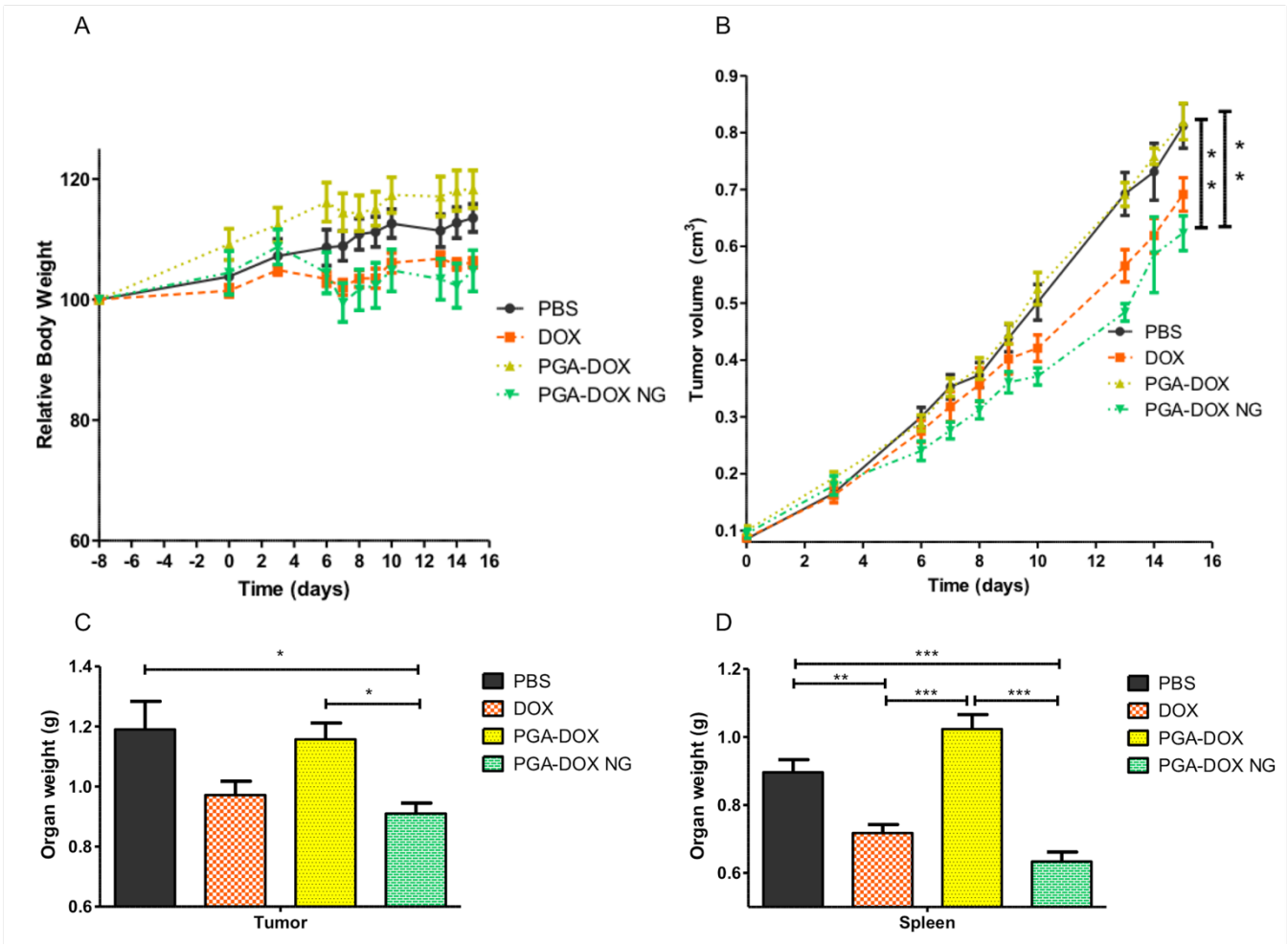

Figure 5. A-B. Safety (**A**) and antitumor activity (**B**) expressed relative to bodyweight of PGA-DOX NG (10 mg/kg DOX-eq) in an orthotopic 4T1 breast tumor mice model in comparison with control (PBS),

free DOX (3 mg/kg DOX-eq), and a PGA-DOX conjugate (10 mg/kg DOX-eq). Treatments were performed at day 0 (tumor volume = 0.1 cm^3), 3, and 6. Animals treated with PGA-DOX NG treatment exhibited a significant reduction in tumor volume (24%) compared to those treated with PBS or PGA-DOX conjugate, with no significant loss in animal weight observed. DOX treatment reduced the tumor volume by up to 14% of PBS treated animals. One-way ANOVA and Bonferroni post hoc were used for comparison between groups at the endpoint. *$P<0.05$. **C-D**. Weight of tumors (**C**) and spleen (**D**) from orthotopic 4T1 breast tumor mice after sacrifice at day 15. Mice treated with PGA-DOX NG showed significant reductions in tumor and spleen weight compared to PBS and PGA-DOX conjugate. One-way ANOVA and Tukey post hoc were used for comparison between groups. *$P<0.05$; **$P<0.01$; ***$P<0.001$.

Splenic and hepatic erythropoiesis-induced acute splenomegaly characterizes this tumor model,[50,51] and represents a collateral impact of tumor development.[48] Encouragingly, both free DOX and PGA-DOX NG significantly reduced splenomegaly, as measured by alterations to spleen weight (Figure 5D).

PGA-DOX NG Treatment Promotes a Near-complete Reduction in Lung and Lymph Node Metastases

Lung and lymph node metastasis represent common complications in breast cancer patients and a particular concern in TNBC. The 4T1 orthotopic tumor model employed within this study develops spontaneous metastasis in the lungs and lymph nodes.[48,50] When analyzing those metastatic sites post-treatment, we discovered that PGA-DOX NGs exerted a very robust anti-metastatic effect in the lungs and the axillary lymph nodes (Figure 6A). We first detected lung micrometastasis around day three after cell inoculation, although we failed to find evident sub-pleural metastases until day 8 (day 0 of our treatment schedule).[48,50] We observed the first signs of lymph node metastasis signs at day 13 (day 5 of our treatment schedule) in a less reproducible pattern when compared to lung metastasis. This lack of uniformity explains the higher variability observed in the determination of axillary lymph node metastasis (Figure 6A right) when compared to lung metastasis (Figure 6A left). We determined the number of 6-thioguanine-resistant metastatic cells in the relevant organs after organ collection and digestion using Trypan Blue staining.[48,52] Results demonstrated (Figure 6A) that PGA-DOX NG treatment significantly inhibited lung

metastases (up to 80%) when compared to control, whereas free DOX failed to exert a significant effect. Moreover, PGA-DOX NG treatment almost completely suppressed axillary lymph node metastasis, while free DOX and the PGA-DOX control conjugate exerted moderate non-statistically significant effects (Figure 6B).

Importantly, lungs from animals treated with PGA-DOX NGs weighed significantly less than lungs from control animals or animals treated with DOX or the PGA-DOX conjugate (Figure 6B). This finding represents another indication of effective anti-metastatic activity and the possible reduction of inflammation, which could inhibit tumor recurrence.
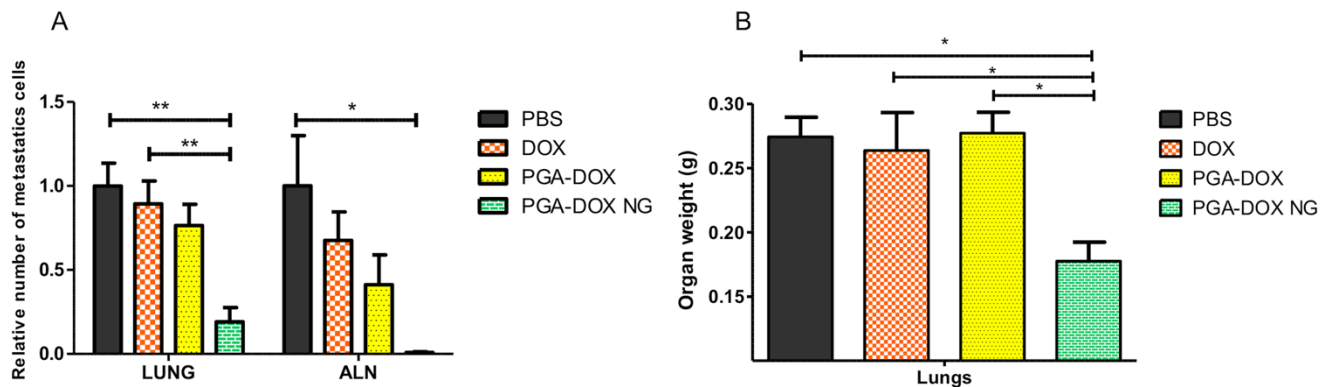
Figure 6. The anti-metastatic activity of PGA-DOX NG in an orthotopic 4T1 breast tumor mice model in comparison with PBS-treated control, free DOX, and the PGA-DOX conjugate, as measured by Trypan Blue staining (**A**). PGA-DOX NGs exerted significant anti-metastatic activity in the lungs (left) when compared to animals treated with PBS, free DOX and control PGA-DOX conjugate. Inhibition of axillary lymph node (ALN) metastasis (right) was also significantly reduced following PGA-DOX NGs when compared to PBS controls. One-way ANOVA and Bonferroni post hoc were used for comparison between groups. *$P<0.05$ and **$P<0.01$ **B**) Weight of lungs extracted from orthotopic 4T1 breast tumor-bearing mice after sacrifice at day 15. Mice treated with PGA-DOX NG displayed a significant reduction in lung weight compared to PBS control, PGA-DOX conjugate, and free DOX treatment, with these findings related to the lower incidence of lung metastases. One-way ANOVA and Tukey post hoc were used for comparison between groups. *$P<0.05$.

The observed anti-metastatic activity, as previously demonstrated with pH-responsive PGA-hyd-DOX conjugates,[48] could result from the rapid DOX release from PGA-DOX NGs (as shown in Figure

3A) due to the presence of cathepsin B already at the tumor extracellular matrix,[53,54] allowing DOX to exert its activity in tumor microenvironment after tumor accumulation by the EPR effect. Additionally, this could be partially explained by NGs size and deformability properties. It has been demonstrated by us and others that soft nanogels with hydrodynamic diameters between 100 and 200 nm have a strong localization in the lungs in the early time points after intravenous administration, as well as in the liver and spleen.[55-57] Metastases result from the activities of multiple orchestrated pathways that provide cancer cells with the ability to migrate, access the bloodstream or lymphatic vessels, and eventually colonize distant sites. Lymph node metastases generally arise through the formation of new lymphatic vessels (lymphangiogenesis),[58,59] whereas metastases to distant organs occur through new blood vessel formation (angiogenesis).[60] The VEGF family proteins, among other important factors, regulate both processes,[61] and studies have positively correlated VEGF expression with tumor size, depth of invasion, lymphatic and venous invasion, and lymph node metastasis. Furthermore, VEGF has even been used for pathological staging and as a marker for recurrence in several cancers.[62,63] Additionally, a recent report suggested the dependence of metastasis on components of the blood coagulation cascade such as thrombin[64-66] or tissue factor (TF), although the exact mechanisms by which this occurs have yet to be fully elucidated. Indeed, studies have discovered TF overexpression in metastatic breast cancer cells when compared to non-metastatic cancer cells.[67]
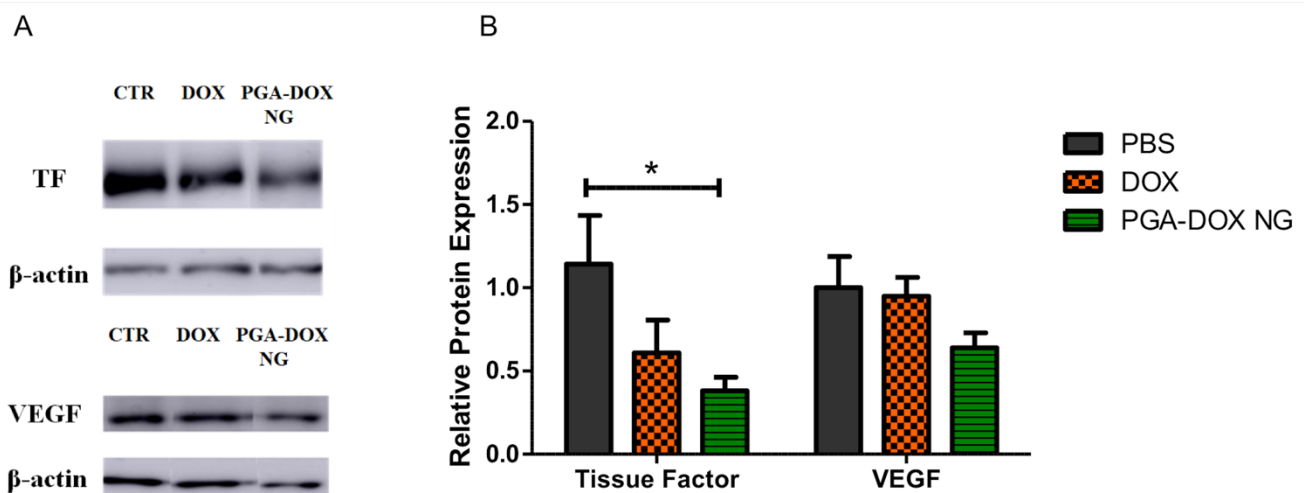
Figure 7. Effect of PGA-DOX NGs treatments in vascular endothelial growth factor (VEGF) and tissue factor (TF) expression in the tumors from orthotopic 4T1 breast tumor mice model using Western blotting (**A**) and quantification with ImageJ (**B**). Results derived from tumor samples extracted at the experimental endpoints compared with untreated controls (PBS) and free DOX. One-way ANOVA and Bonferroni post hoc were used for comparison between groups. $*P<0.05$.

Results from Western blotting analyses (Figure 7) highlighted the significant decrease in TF expression in tumors deriving from PGA-DOX NG treated animals compared to the PBS control, but not when compared to free DOX; however, PGA-DOX NG treatment although showed a clear trend, failed to induce the significant inhibition of VEGF expression in tumors. These preliminary results suggest that the mechanism of action of our PGA-DOX NGs includes an important anti-metastatic component; therefore, we could specifically target metastases in distant organs through the implementation of the injectable PGA-DOX NGs.

Conclusions

In this study, we report on the development of a new drug delivery platform comprising the first example of anionic chemically-crosslinked nanogels (NGs) exclusively formed from biodegradable and biocompatible polypeptides, in particular polyglutamates (PGA). We employed copper-catalyzed azide-alkyne cycloaddition (CuAAC) to prepare NGs in inverse miniemulsion with orthogonally derivatized PGAs, thus allowing control over size and dispersity. These bioresponsive PGA-DOX NGs displayed robust uptake by 4T1 cancer cells and significant DOX release when incubated with the enzyme Cathepsin B, thereby suggesting their potential therapeutic efficacy in TNBC treatment. Following PGA-DOX NG treatment in an orthotopic TNBC murine model, we observed a reduction in primary tumor growth and a significant reduction in lung and lymph node metastasis without any noted side toxicities. We also undertook a preliminary mechanistic exploration that provides evidence of a potential modulation of the molecular mechanisms ruling metastatic progression. With further developments, we believe that this anti-

metastatic NG platform may represent a powerful tool for the treatment of advanced-stage breast cancer, such as many TNBC cases where primary tumor resection is not sufficient to block cancer progression.

Supporting Information

Materials, Methods for Physico-chemical Characterization and Biological Evaluation, Supplementary Figures, and Supplementary Tables can be found in the Electronic Supplementary Information (ESI).

Author Contributions

A.D-C, A. S-H, M.C., and M.J.V. developed the concept and design of the project. Synthesis and physic-chemical characterization steps were performed by A.D-C and A.S-H. Drug-release profiles were performed by A.S-H. Cell assays were performed by A.D-C. *In vivo* experiments were performed by A.A., A.D-C, D.C., and J.J.A-C. Analysis and interpretation of the data included the contribution of all authors. The manuscript was written by A.D-C and A.S-H. and revised by M.C. and M.J.V. All authors have given approval for the final version of the manuscript.

Notes

The authors declare no competing financial interests.

ABBREVIATIONS

AFM, Atomic Force Microscopy, CD, Circular Dichroism; Dh, Hydrodynamic Diameter; DLC, Drug Loading Content; DLE, Drug Loading Efficiency; DLS, Dynamic Light Scattering; DOX, Doxorubicin; FT-IR, Fourier Transform Infrared Spectroscopy; NMR, Nuclear Magnetic Resonance; PBS, Phosphate Buffer Saline; PGA, Poly(glutamic acid); PI, propidium iodide; SEM, Scanning Electron Microscopy; TEM, Transmission Electron Microscopy; TF, Tissue Factor; TNBC, Triple Negative Breast Cancer; UV-VIS, Ultraviolet-Visible; VEGF, Vascular Endothelial Growth Factor.

References

1. Yadav, H. K., Halabi, A. & Alsalloum, N. A. *Nanogels as Novel Drug Delivery Systems-A Review*. *J Pharm Pharm Res* **1**, (2017).

2. Asadian-Birjand, M., Sousa-Herves, A., Steinhilber, D., Cuggino, J. C. & Calderon, M. Functional Nanogels for Biomedical Applications.

3. Cuggino, J. C., Blanco, E. R. O., Gugliotta, L. M., Alvarez Igarzabal, C. I. & Calderón, M. Crossing biological barriers with nanogels to improve drug delivery performance. *Journal of Controlled Release* **307**, 221–246 (2019).

4. Kabanov, A. V. & Vinogradov, S. V. Nanogels as pharmaceutical carriers: Finite networks of infinite capabilities. *Angewandte Chemie - International Edition* **48**, 5418–5429 (2009).

5. Vicario-de-la-Torre, M. & Forcada, J. The Potential of Stimuli-Responsive Nanogels in Drug and Active Molecule Delivery for Targeted Therapy. *Gels* **3**, 16 (2017).

6. Ganta, S., Devalapally, H., Shahiwala, A. & Amiji, M. A review of stimuli-responsive nanocarriers for drug and gene delivery. *Journal of Controlled Release* **126**, 187–204 (2008).

7. Zhang, X., Malhotra, S., Molina, M. & Haag, R. Micro- and nanogels with labile crosslinks-from synthesis to biomedical applications. *Chemical Society Reviews* **44**, 1948–1973 (2015).

8. Kar, M. *et al.* Chapter 12: Responsive Nanogels for Anti-cancer Therapy. in *RSC Smart Materials* **2018-January**, 210–260 (Royal Society of Chemistry, 2018).

9. Klinger, D., Aschenbrenner, E. M., Weiss, C. K. & Landfester, K. Enzymatically degradable nanogels by inverse miniemulsion copolymerization of acrylamide with dextran methacrylates as crosslinkers. *Polym. Chem.* **3**, 204–216 (2012).

10. Nagel, G., Sousa-Herves, A., Wedepohl, S. & Calderón, M. Matrix metalloproteinase-sensitive multistage nanogels promote drug transport in 3D tumor model. *Theranostics* **10**, 91–108 (2020).

11. Ekkelenkamp, A. E., Elzes, M. R., Engbersen, J. F. J. & Paulusse, J. M. J. Responsive crosslinked polymer nanogels for imaging and therapeutics delivery. *Journal of Materials Chemistry B* **6**, 210–

235 (2018).

12. Duro-Castano, A., Conejos-Sánchez, I. & Vicent, M. Peptide-Based Polymer Therapeutics. *Polymers (Basel).* **6**, 515–551 (2014).

13. Ekladious, I., Colson, Y. L. & Grinstaff, M. W. Polymer–drug conjugate therapeutics: advances, insights and prospects. *Nature Reviews Drug Discovery* **18**, 273–294 (2019).

14. Nishimura, T. *et al.* Self-Assembled Polypeptide Nanogels with Enzymatically Transformable Surface as a Small Interfering RNA Delivery Platform. *Biomacromolecules* **18**, 3913–3923 (2017).

15. Yang, J. *et al.* Poly-Î 3-glutamic acid/chitosan nanogel greatly enhances the efficacy and heterosubtypic cross-reactivity of H1N1 pandemic influenza vaccine. *Sci. Rep.* **7**, (2017).

16. Xing, T., Lai, B. & Yan, L. Disulfide Cross-Linked Polypeptide Nanogel Conjugated with a Fluorescent Probe as a Potential Image-Guided Drug-Delivery Agent. *Macromol. Chem. Phys.* **214**, 578–588 (2013).

17. Shi, F. *et al.* Intracellular microenvironment responsive PEGylated polypeptide nanogels with ionizable cores for efficient doxorubicin loading and triggered release. *J. Mater. Chem.* **22**, 14168–14179 (2012).

18. Shi, B. *et al.* Intracellularly swollen polypeptide nanogel assists hepatoma chemotherapy. *Theranostics* **7**, 703–716 (2017).

19. Li, S. *et al.* Sarcoma-targeting peptide-decorated polypeptide nanogel intracellularly delivers shikonin for upregulated osteosarcoma necroptosis and diminished pulmonary metastasis. *Theranostics* **8**, 1361–1375 (2018).

20. Bianchini, G., Balko, J. M., Mayer, I. A., Sanders, M. E. & Gianni, L. Triple-negative breast cancer: Challenges and opportunities of a heterogeneous disease. *Nature Reviews Clinical Oncology* **13**, 674–690 (2016).

21. Xiao, W. *et al.* Risk factors and survival outcomes in patients with breast cancer and lung metastasis: a population-based study. *Cancer Med.* **7**, 922–930 (2018).

22. Farnsworth, R. H., Achen, M. G. & Stacker, S. A. The evolving role of lymphatics in cancer metastasis. *Curr. Opin. Immunol.* **53**, 64–73 (2018).

23. Stacker, S. A., Achen, M. G., Jussila, L., Baldwin, M. E. & Alitalo, K. Lymphangiogenesis and cancer metastasis. *Nature Reviews Cancer* **2**, 573–583 (2002).

24. Rostovtsev, V. V., Green, L. G., Fokin, V. V. & Sharpless, K. B. A stepwise huisgen cycloaddition process: Copper(I)-catalyzed regioselective 'ligation' of azides and terminal alkynes. *Angew. Chemie - Int. Ed.* **41**, 2596–2599 (2002).

25. Barz, M., Duro-Castano, A. & Vicent, M. J. A versatile post-polymerization modification method for polyglutamic acid: synthesis of orthogonal reactive polyglutamates and their use in "click chemistry". *Polym. Chem.* **4**, 2989 (2013).

26. Sousa-Herves, A., Wedepohl, S. & Calderón, M. One-pot synthesis of doxorubicin-loaded multiresponsive nanogels based on hyperbranched polyglycerol. *Chem. Commun.* **51**, 5264–5267 (2015).

27. Duro-Castano, A. *et al.* Well-defined star-shaped polyglutamates with improved pharmacokinetic profiles as excellent candidates for biomedical applications. *Mol. Pharm.* **12**, 3639–3649 (2015).

28. Sousa-Herves, A., Sánchez Espinel, C., Fahmi, A., González-Fernández, Á. & Fernandez-Megia, E. In situ nanofabrication of hybrid PEG-dendritic-inorganic nanoparticles and preliminary evaluation of their biocompatibility. *Nanoscale* **7**, 3933–3940 (2015).

29. Carbinatto, F. M., de Castro, A. D., Evangelista, R. C. & Cury, B. S. F. Insights into the swelling process and drug release mechanisms from cross-linked pectin/high amylose starch matrices. *Asian J. Pharm. Sci.* **9**, 27–34 (2014).

30. Bukhari, S. M. H., Khan, S., Rehanullah, M. & Ranjha, N. M. Synthesis and Characterization of Chemically Cross-Linked Acrylic Acid/Gelatin Hydrogels: Effect of pH and Composition on Swelling and Drug Release. *Int. J. Polym. Sci.* **2015**, (2015).

31. Kim, J. O., Kabanov, A. V. & Bronich, T. K. Polymer micelles with cross-linked polyanion core for delivery of a cationic drug doxorubicin. *J. Control. Release* **138**, 197–204 (2009).

32. Li, M. *et al.* Nanoscaled poly(l-glutamic acid)/doxorubicin-amphiphile complex as pH-responsive drug delivery system for effective treatment of nonsmall cell lung cancer. *ACS Appl. Mater. Interfaces* **5**, 1781–1792 (2013).

33. Cunningham, A. J., Robinson, M., Banquy, X., Leblond, J. & Zhu, X. X. Bile Acid-Based Drug Delivery Systems for Enhanced Doxorubicin Encapsulation: Comparing Hydrophobic and Ionic Interactions in Drug Loading and Release. *Mol. Pharm.* **15**, 1266–1276 (2018).

34. Duro-Castano, A. *et al.* Capturing "Extraordinary" Soft-Assembled Charge-Like Polypeptides as a Strategy for Nanocarrier Design. *Adv. Mater.* **29**, 1702888 (2017).

35. Gallois, L., Fiallo, M. & Garnier-Suillerot, A. Comparison of the interaction of doxorubicin, daunorubicin, idarubi-cin and idarubicinol with large unilamellar vesicles: Circular dichroism study. *Biochimica et Biophysica Acta (BBA) – Biomembranes* **1370** (1), 31-40 (1998).

36. Shaffer, S. A. *et al.* In vitro and in vivo metabolism of paclitaxel poliglumex: identification of metabolites and active proteases. *Cancer Chemother. Pharmacol.* **59**, 537–48 (2007).

37. Chiu, H. C., Kopečková, P., Deshmane, S. S. & Kopeček, J. Lysosomal degradability of poly(α-amino acids). *J. Biomed. Mater. Res.* **34**, 381–392 (1997).

38. Melancon, M. P. *et al.* A novel method for imaging in vivo degradation of poly(L-glutamic acid), a biodegradable drug carrier. *Pharm. Res.* **24**, 1217–1224 (2007).

39. Kos, J., Werle, B., Lah, T. & Brunner, N. Cysteine proteinases and their inhibitors in extracellular fluids: Markers for diagnosis and prognosis in cancer. in *International Journal of Biological Markers* **15**, 84–89 (Wichtig Editore s.r.l., 2000).

40. Lah, T. T. *et al.* Cells producing cathepsins D, B, and L in human breast carcinoma and their association with prognosis. in *Human Pathology* **31**, 149–160 (W.B. Saunders, 2000).

41. Obst, K. *et al.* Protein Corona Formation on Colloidal Polymeric Nanoparticles and Polymeric Nanogels: Impact on Cellular Uptake, Toxicity, Immunogenicity, and Drug Release Properties. *Biomacromolecules* **18**(6), 1762–1771 (2017).

42. Blanco, E., Shen, H. & Ferrari, M. Principles of nanoparticle design for overcoming biological barriers to drug delivery. *Nature Biotechnology* **33**, 941–951 (2015).

43. Trouet, A., Deprez-de Campeneere, D., & De Duve, C. Chemotherapy through lysosomes with a DNA-daunorubicin complex. *Nature New Biol.* **239**, 110–112 (1972).

44. Duncan, R., Richardson, SCW. Endocytosis and intracellular trafficking as gateways for nano-medicine delivery: opportunities and challenges. *Mol Pharm*. **9**, 2380–2402 (2012).

45. De Duve, C., De Barsy, T., Poole, B., *et al*. Lysosomotropic agents. Biochem Pharmacol. **23**, 2495–2531 (1974).

46. Lüpertz, R., Wätjen, W., Kahl, R. & Chovolou, Y. Dose- and time-dependent effects of doxorubicin on cytotoxicity, cell cycle and apoptotic cell death in human colon cancer cells. *Toxicology* **271**, 115–121 (2010).

47. Zagorodko, O., Arroyo-Crespo, J. J., Nebot, V. J. & Vicent, M. J. Polypeptide-Based Conjugates as Therapeutics: Opportunities and Challenges. *Macromol. Biosci.* **201600316**, 1–22 (2016).

48. Arroyo-Crespo, J. J. *et al.* Tumor microenvironment-targeted poly-L-glutamic acid-based combination conjugate for enhanced triple negative breast cancer treatment. *Biomaterials* **186**, 8–21 (2018).

49. Arroyo-Crespo, J. J. *et al.* Anticancer Activity Driven by Drug Linker Modification in a Polyglutamic Acid-Based Combination-Drug Conjugate. *Adv. Funct. Mater.* **28**, 1800931 (2018).

50. Arroyo-Crespo, J. J. *et al.* Characterization of triple-negative breast cancer preclinical models provides functional evidence of metastatic progression. *Int. J. Cancer* **145**, 2267–2281 (2019).

51. Liu, M. *et al.* Macrophages support splenic erythropoiesis in 4T1 tumor-bearing mice. *PLoS One* **10**, (2015).

52. Pulaski, B. A. & Ostrand-Rosenberg, S. Mouse 4T1 Breast Tumor Model. *Curr. Protoc. Immunol.* **39**, (2000).

53. Whitana, N.P. et al. Cathepsin B Inhibition Limits Bone Metastasis in Breast Cancer *Cancer Res* **72**,1199-1209 (2012).

54. Sloane, B.F. et al. Cathepsin B and tumor proteolysis: contribution of the tumor microenvironment *Seminars in Cancer Biology* **15**(12),149-157 (2005)

55. Theune, L.E. *et al.* NIR- and thermo-responsive semi-interpenetrated polypyrrole nanogels for imaging guided combinational photothermal and chemotherapy. *J. Control Release* **311-312**, 147-161 (2019).

56. Gordon, M.R. *et al.* Biodistribution Analysis of NIR-Labeled Nanogels Using in Vivo FMT Imaging in Triple Negative Human Mammary Carcinoma Models. *Mol Pharm* **15**(3),1180-1191 (2018).

57. Lux, J., White, A.G., Chan, M., Anderson, C.J., Almutairi, A. Nanogels from Metal-Chelating Crosslinkers as Versatile Platforms Applied to Copper-64 PET Imaging of Tumors and Metastases. *Theranostics* **5**(3), 277-288 (2015)

58. Achen, M. G., McColl, B. K. & Stacker, S. A. Focus on lymphangiogenesis in tumor metastasis. *Cancer Cell* **7**, 121–127 (2005).

59. Karpanen, T. & Alitalo, K. Lymphatic vessels as targets of tumor therapy. *Journal of Experimental Medicine* **194**, (2001).

60. Weis, S. M. & Cheresh, D. A. Tumor angiogenesis: Molecular pathways and therapeutic targets. *Nature Medicine* **17**, 1359–1370 (2011).

61. Adams, R. H. & Alitalo, K. Molecular regulation of angiogenesis and lymphangiogenesis. *Nature Reviews Molecular Cell Biology* **8**, 464–478 (2007).

62. Matsui, J. *et al.* Multi-kinase inhibitor E7080 suppresses lymph node and lung metastases of human mammary breast tumor MDA-MB-231 via inhibition of vascular endothelial growth factor-receptor (VEGF-R) 2 and VEGF-R3 kinase. *Clin. Cancer Res.* **14**, 5459–5465 (2008).

63. Choi, W. W. L. *et al.* Angiogenic and lymphangiogenic microvessel density in breast carcinoma: Correlation with clinicopathologic parameters and VEGF-family gene expression. *Mod. Pathol.* **18**, 143–152 (2005).

64. Belting, M., Ahamed, J. & Ruf, W. Signaling of the tissue factor coagulation pathway in angiogenesis and cancer. *Arteriosclerosis, Thrombosis, and Vascular Biology* **25**, 1545–1550 (2005).

65. Bourcy, M. *et al.* Tissue factor induced by epithelial-mesenchymal transition triggers a procoagulant state that drives metastasis of circulating tumor cells. *Cancer Res.* **76**, 4270–4282 (2016).

66. Remiker, A. S. & Palumbo, J. S. Mechanisms coupling thrombin to metastasis and tumorigenesis. *Thromb. Res.* **164**, S29–S33 (2018).

67. Ueno, T., Toi, M., Koike, M., Nakamura, S. & Tominaga, T. Tissue factor expression in breast cancer tissues: Its correlation with prognosis and plasma concentration. *Br. J. Cancer* **83**, 164–170 (2000).

Table of Contents artwork
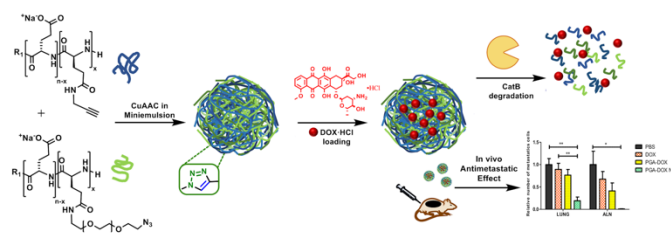
Supporting Information for

Polyglutamic acid-based Crosslinked Doxorubicin Nanogels as an Anti-Metastatic Treatment for Triple Negative Breast Cancer

Aroa Duro-Castano[†,I], Ana Sousa-Herves[‡,I], Ana Armiñán[†], David Charbonnier[†], Juan José Arroyo-Crespo[†], Stefanie Wedepohl[‡], Marcelo Calderón[§,⊥], María J. Vicent[†*]*

[†]Polymer Therapeutics Lab, Centro de Investigación Príncipe Felipe, Eduardo Primo Yúfera 3, 46012 Valencia, Spain

[‡]Freie Universität Berlin, Institut für Chemie und Biochemie, Takustrasse 3, 14195 Berlin, Germany

[§]POLYMAT & Applied Chemistry Department, Faculty of Chemistry, University of the Basque Country UPV/EHU, Paseo Manuel de Lardizabal 3, 20018, Donostia-San Sebastián, Spain

[⊥]IKERBASQUE, Basque Foundation for Science, 48013 Bilbao, Spain

Table of Contents

5. Additional Supplementary Figures

1. Materials

All chemicals were reagent grade, obtained from Sigma- Aldrich, and used without further purification unless otherwise indicated. Poly (L-glutamic acid) (PGA) MW=10,500 Da, PDI 1.1 was purchased from Polypeptide Therapeutic Solutions (PTS, Valencia, Spain). Phenazine methosulfate (PMS), sodium citrate, and triton were supplied by Sigma (Spain). Dulbecco's Modified Eagle's Medium (DMEM), Leibovitz's L-15 medium, phosphate buffer saline (PBS), fetal bovine serum (FBS) Medium 200, low serum growth supplement (LSGS), and trypsin were purchased from Gibco. 3-(4,5-dimethylthiazol-2-yl)-5- (3-carboxymethoxyphenyl)-2-(4-sulfophenyl)-2H-tetrazolium (MTS) was supplied by Promega (Spain). Doxorubicin hydrochloride (DOX·HCl) was purchased from Yick-Vic Chemicals & Pharmaceuticals (China). Cathepsin B (CatB) from bovine spleen (lyophilized powder, ≥10 units/mg protein), Annexin V, and Propidium Iodide were obtained from Inmunostep (Spain). All solvents were of analytical grade and were used as received or dried and freshly distilled. Ultrapure water with a resistivity of 18 MΩ.cm was used in all aqueous preparations (MilliQ, Millipore). Chloroform-d1, dimethylsulfoxide-d6, and deuterium oxide were purchased from Deutero GmbH (Germany). Preparative size-exclusion chromatography (SEC) was performed using Sephadex G-25 superfine and PD MiniTrap G-10 ™ columns containing 2.1 ml of Sephadex™ G-10 (GE Healthcare, Spain). Dialysis was performed using Amicon Ultra-15 centrifugal tubes fitted with a 1, 3, 10, 30, 50, or 100 kDa molecular weight cut-off (MWCO) regenerated cellulose membrane (Vivaspin®). Formvar precoated copper grids (400 mesh) were bought from Aname S. L (Spain). The 4T1 cell line was obtained from the ATTC®. 6-8 weeks female Balb/c mice used for all the experimental procedures were purchased from Harlan Laboratories Inc. (Spain).

2. Physico-Chemical Characterization

NMR Spectroscopy. NMR spectra were recorded at 27°C (300K) on a Bruker AC 300 or Bruker DRX 500 spectrometer. Data were processed with the software Mestrenova 6.2. Samples were prepared at the desired concentration in D_2O.

Circular Dichroism. CD Spectroscopy was performed with a J-815 CD Spectrometer (JASCO Corporation) using a Peltier thermostated cell holder (PTC-423, JASCO Corporation) with a recirculating cooler (JULABO F250, JASCO Corporation). A nitrogen flow (~2.7 L/min) was led through the spectrometer and controlled with a nitrogen flow monitor (Afriso Euro-Index). The samples were dissolved in double-distilled water (MilliQ H_2O) at 0.1 mg/mL. Samples were measured repeatedly (n= 3) in a quartz cuvette with d= 0.1 cm.

Dynamic Light Scattering. DLS measurements were performed using a Malvern Zetasizer NanoZS instrument equipped with a 532 nm laser at a fixed scattering angle of 173°. Solutions of the polymers at 1 mg/mL in PBS (to mimic physiological environment) were sonicated for 10 min and allowed to equilibrate for the required time, filtered through a 0.45 μm cellulose membrane filter, and measured. Size distribution was measured (radius, nm) for each compound per triplicate with n> 3 measurements. Automatic optimization of beam focusing and attenuation were applied for each sample.

Z-Potential Measurements. Z-potential measurements were performed at 20°C using a Malvern Zetasizer NanoZS instrument, equipped with a 532nm laser using Disposable folded capillary cells (Malvern Instruments Ltd, Worcestershire, UK). Polymer solutions were prepared in 10 mM PBS pH 7.4. The solutions were filtered through a 0.45 μm cellulose membrane filter. Z-potential was measured for each sample per triplicate with n> 3 measurements.

Fourier Transform Infrared Spectroscopy. IR spectra were recorded using Thermo Scientific Nicolet 380 FT-IR spectrometer with a spectral range 7800-350 cm-1, optical resolution (apodized) < 0.9

cm^{-1} resolution (standard) and peak-to-peak noise < 2.2·10-5 abs. (> 22000:1) (1-minute scan). All samples analyzed were under solution or previously dissolved in DMF. The analysis was carried out at 25 ˚C.

Ultraviolet-Visible Spectroscopy. UV-VIS measurements were performed using JASCO V-630 spectrophotometer at 25°C with 1.0 cm matched quartz cells and with a spectral bandwidth of 0.5 nm. In the case of nanogels, a Perkin Elmer Lambda 750 Spectrophotometer was employed.

Scanning Electron Microscopy. SEM micrographs of the nanogels were acquired using a Quanta 200 FEG Environmental SEM, in high vacuum with an accelerating voltage of 5.0 KV. A droplet of nanogel solution was placed onto the surface of a silicon wafer, air-dried for 20 mins, and then covered with a 4 nm layer of chromium.

Atomic Force Microscopy. A nanogel droplet was placed on a Mica sheet and allowed to dry overnight. AFM imaging was performed in air using a MultiMode 8 AFM equipped with a NanoScope V system (Veeco, Santa Barbara, USA) operated in tapping mode. Samples were analyzed using NanoWorld tips, Non-Contact/Tapping Mode-Long Cantilever (NCL-W), with a resonance frequency of 190 kHz and constant force of 48 N m^{-1}. Statistical analyses were performed using NanoScope Analysis 1.3 software in a 5 x 5 μm image. Total Count: 514.00. Diameter: 98.16 nm. SD: 30.57 nm

Cryo-Transmission Electron Microscopy. Specimens for the cryo-TEM observation of vitreous thin films were prepared using a "cryoplunge" cryo-fixation device (Leica EM GP, Germany), which enables rapid immersion in a cryogenic fluid (liquid ethane or propane). A typical support is a TEM copper grid (3 mm in diameter) recovered with a Lacey-type carbon film that contains regularly or randomly dispersed holes in which the aqueous dispersion is placed (Ted Pella Inc., USA). A glow discharged treatment is applied to the carbon film to render it hydrophilic, before the deposition of a 5 μl microdrop of the dispersion that is reduced in thickness by blotting with Whatman paper. The liquid film is placed in a

humidity-controlled chamber (which maintains a relative humidity of 97-99%) to prevent its evaporation until the TEM grid is projected into a cold liquid to enable the most efficient absorption of the sample heat. This liquid is ethane that has previously liquefied from gas by placing it in contact with the cold walls of a metal goblet plunged into liquid nitrogen. The direct use of liquid nitrogen is usually avoided because heat transfer is restricted by the existence of a thin intermediate layer of gas (the Leindenfrost effect). 2.5 ml of liquid ethane maintained at -174 °C are sufficient for sample preparation. Below this temperature, liquid ethane solidifies (at around -182.5°C), and while above this temperature, water crystallizes (at around -135°C). Finally, the objects of interest in the aqueous dispersion were embedded in the vitreous water film through the holes in the carbon film support. The TEM grids were mounted on a Gatan 626 Single Tilt Liquid Nitrogen Cryo Transfer Holder (Gatan, USA) equipped with a liquid nitrogen reservoir, and then transferred to the microscope (FEI, Tecnai Spirit G2) using a CT-3500 cryotransfer system (Gatan, USA) designed to ensure that the frozen state of the sample is uninterrupted.

3. Optimization of Polyglutamic Acid-based Nanogel Synthesis

a) PGA Precursors Synthesis

Alkyne and azide derivatized PGAs were synthesized in a previous step, according to Barz et al.[1] and using a PGA of Mw 10,500 Da and PDI 1.1. We employed propargylamine and oligoethylene glycol azide residues for the alkyne and azide functionalization, respectively, to yield compounds S1-S5 (see Scheme S1 and Table S1).

a) Poly(glutamic acid-co-EG(n)N_3 glutamate), **1, 2** and **5**: ^{1}H NMR δH (300MHz, D2O): 4.28-4.07 (1H, m), 3.65-3.51 (xH, m), 3.48 (2xH, t), 3.40-3.30 (2xH, m), 3.25 (2xH, d), 2.29 -2.00(2H, m), 1.98 - 1.65 (2H, m). *R: 8 for EG2, 20 for EG6. x: molar percentage of modification.

b) Poly(glutamic acid-co-propargyl glutamate), **3-4**: ^{1}H NMR δH (300MHz, D2O): 4.30-4.02 (1H, m), 3.81 (2xH, s), 2.48 (1xH, s), 2.35-2.02 (2H, m), 2.01-1.65 (2H, m). x: molar percentage of modification.
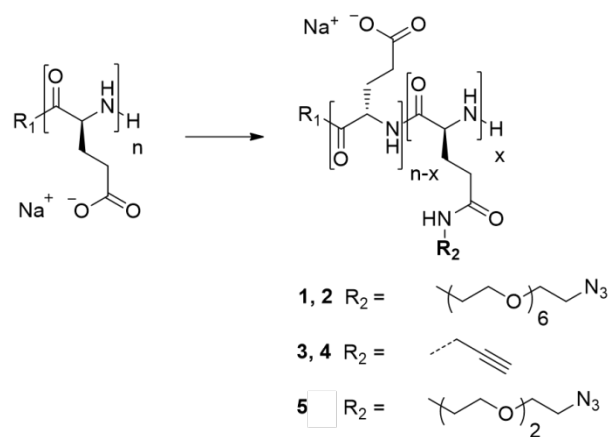
Scheme 1. Alkyne and Azide functionalization of PGA.

Table S1. Alkyne and Azide PGA precursors.

Compound	Description	% Alkyne/Azide*	MW KDa#
1	PGA-coPGAPEG(6)N$_3$	10	12.7
2	PGA-coPGAPEG(6)N$_3$	17	14.3
3	PGA-coPGAPropargyl	10	10.7
4	PGA-coPGAPropargyl	17	10.7
5	PGA-coPGAPEG(2)N$_3$	18	12.8

* Obtained by ^{1}H-NMR, # calculated theoretically.

b) Preparation of PGA NGs and DOX Loading
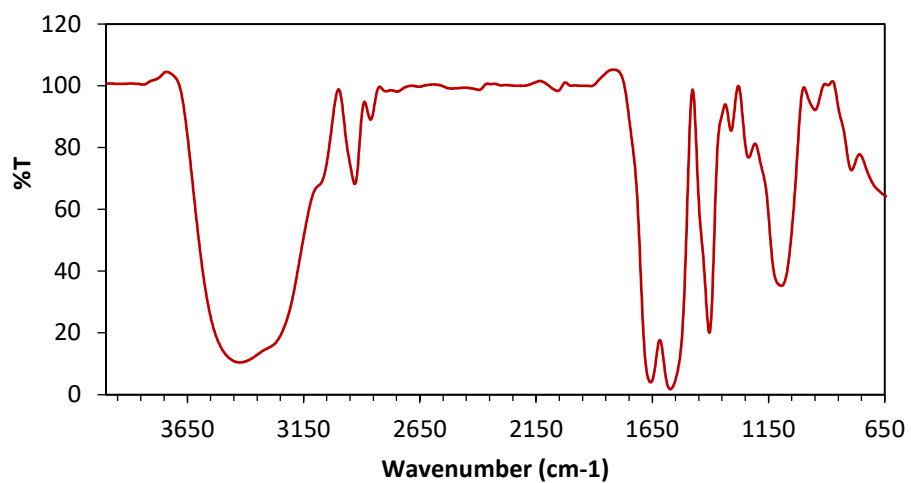
Figure S1 Representative FT-IR-spectra of NG 1 (Table 2) confirming the disappearance of the azide asymmetric stretching band at 2124 cm^{-1}.
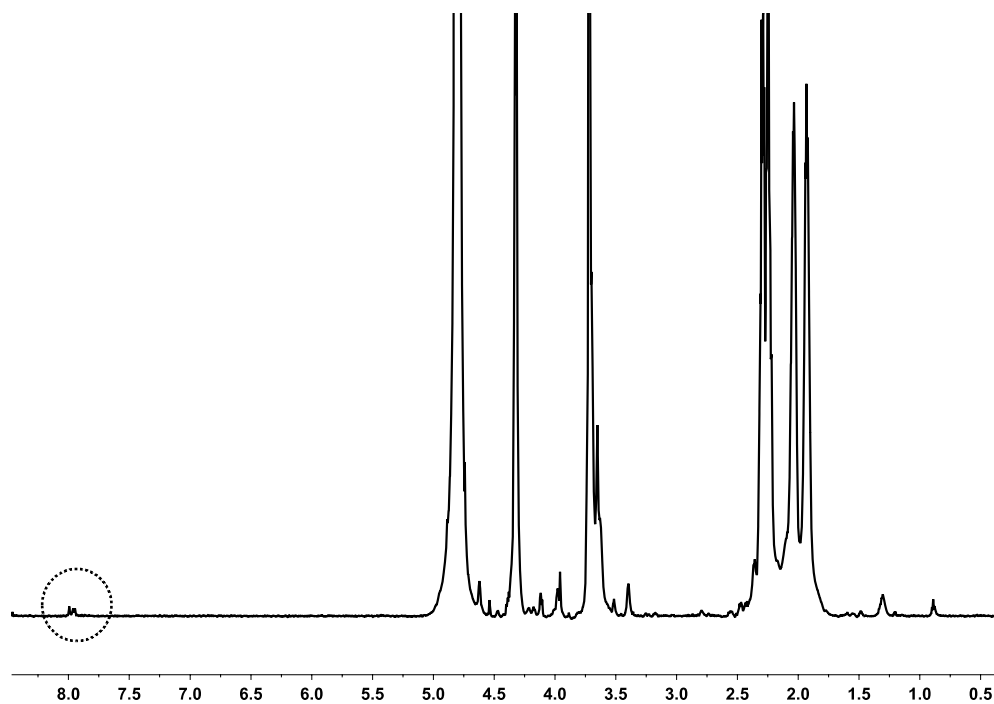

Figure S2. ^{1}H NMR spectrum (D$_2$O) of PGA NG showing the formation of the triazole rings around 8 ppm.

$$DLC\ (wt.\%) = \frac{amount\ of\ drug\ in\ nanogel}{amount\ of\ drug - loaded\ nanogel}x100$$

Equation 1. Drug loading content (DLC)

$$DLC\ (wt.\%) = \frac{amount\ of\ drug\ in\ nanogel}{total\ amount\ of\ feeding\ drug}x100$$

Equation 2. Drug loading efficiency (DLE)

c) Copper Removal Efficiency and Related Cytotoxicity

To remove copper catalyst traces, a previously described procedure for CuAAC coupling of polymers with carboxylic acids was followed [2]. Briefly, during the aqueous purification, the NGs were washed with a solution of aq. HCl pH 3 (2 × 30 ml), followed by saturated $NaHCO_3$ (2 × 30 ml), and finally with H_2O (4 × 30 ml). The acidic conditions should protonate the carboxylic acid groups, therefore hampering their complexation with remaining copper ions. To probe the efficiency of this procedure, MTT assays of the NGs washed either only with H_2O or submitted to acidic treatment were carried out. As depicted in Figure S3, a remarkably lower level of toxicity was observed for those NGs submitted to the copper removal treatment. Cell viability was assessed after 48 h exposure to different dilutions of the compounds to cells by MTT test. A549 cells were obtained from the Leibnitz Institute DSMZ – German Collection of Microorganisms and Cell Cultures and were routinely grown at 37°C and 5% CO_2 in DMEM (Thermo Fisher Scientific) with 10% FBS (FBS Superior, Merck) and 1% penicillin/streptomycin (Thermo Fisher Scientific). 10,000 cells/well were seeded into 96 well plates and grown overnight. The next day, the medium was removed and replaced with 100 µL/well fresh medium containing 10-fold serial dilutions of the test compounds and incubated for 48 h at 37 °C and 5% CO_2. Then, the supernatant was removed, and 100 µL/well fresh medium containing 10µL per well MTT (5 mg/ml in PBS, Millipore Sigma) was added and incubated for 4 h at 37 °C, removed again, and the formazan crystals were dissolved in 100

µL/well isopropanol with 0.04 M HCl while shaking. Absorbance was read at 570 nm in a Tecan Infinite M200 Pro microplate reader. Average absorbance values from duplicate wells of cells treated with the test compounds were divided by average absorbance values of wells containing untreated cells to obtain relative viability values. Tests were repeated at least three times independently to calculate errors.
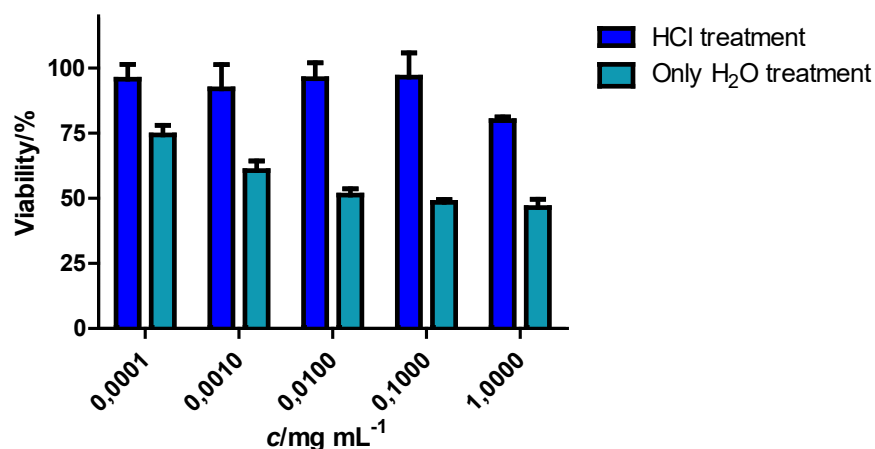

Figure S3. Cytotoxicity of PGA NGs with and without copper removal treatment against A549 cells measured by MTT assay

4. Biological Methods

Cell Culture protocols. 4T1 cells were cultured in RPMI-1640 media supplemented with 10% FBS. Cells were maintained at 37°C in an atmosphere of 5% carbon dioxide and 95% air. The medium was replaced every 2-3 days and underwent passage once weekly when 80% of cell confluence was reached.

MTS assay for Cell Viability. Cells were seeded in sterile 96-well microtitre plates at a cell density of 6,250 cells/cm^2 for 4T1. Plates were incubated for 24 h, and compounds (sterilized under UV-light) were then added to give a final concentration of 0.01 to 50 µg/mL eq-DOX (0.4 to 200 µg/mL polymer). After 72 h of incubation, MTS/PMS (20:1) (10 µL of manufacturer solution) was added to each well, and

the cells were incubated for a further 2 h. The optical density of each well was measured at 490 nm. Plates were read spectrophotometrically using a Victor2Wallac^{TM} plate reader. The absorbance values were represented as the percentage of cell viability taken as 100% cell viability of untreated control cells. N>4 independent experiments, with 6 replicates each.

Cellular Uptake by Flow Cytometry. 4T1 cells were seeded in 6-well plates at a density of 6,900 cell/cm^2 (1 ml cell suspension per well) and allowed to adhere for 24 h. In binding experiments conducted at 4°C, cells were pre-incubated at this temperature for 30 min before the start of the experiment. For both experiments, 4°C and 37°C, the cathepsin B inhibitor CA-074 (0.4 μL from a solution of 5 μM to reach a final concentration of 2 μM) was added 30 min before the addition of the NG. Then, 10 μL of DOX-loaded NG (12 μg/mL eq. DOX final concentration) were added at different time points from 0 to 300 min. Meanwhile, cells were incubated either at 37°C or 4°C for each experiment. Finally, cells were placed on ice to stop energy-dependent mechanisms and washed twice with cold PBS-BSA 0.1%. (PBS supplemented with Bovine Serum Albumin (BSA)). Then cells were suspended in 0.5 ml of cold PBS using a scraper. Finally, the cell pellet was placed in flow cytometer tubes. Cell-associated fluorescence was then analyzed using a Becton Dickinson FACS Calibur cytometer (California, USA) equipped with an argon laser (488 nm) and emission filter for 550 nm. Data collection involved 10,000 counts per sample, and data were analyzed using CELLQuestTM version 3.3 software. Data are expressed by plotting the cell-associated fluorescence, which is the result of the % of positive cells by multiplied by the mean fluorescence. CAF= % positive cells*mean fluorescence/100. Cells incubated without polymer were used to account for the background fluorescence.

Statistical Analysis. Data from the experiments were analyzed using two-way ANOVA and Bonferroni post hoc. In all cases, we considered differences to be significant when p***<0.001; p**<0.01; p*<0.05; ns: non-significant.

Confocal Fluorescence Microscopy for Live-cell Imaging. For live-cell imaging, 4T1 cells were seeded in 6-well plates at a density of 6,900 cell/cm^2 (1 ml cell suspension per well) on glass-bottom culture dishes (1 cm^2 Petri plate) and allowed to seed for 24 h at 37°C. First, the cathepsin B inhibitor CA-074 (0.4μL from a solution of 5 μM to reach a final concentration of 2 μM) was added 30 min prior to the addition of the NG. Then, 10μL of DOX-loaded NG (12 μg/mL eq DOX final concentration), as well as the equivalent concentration of DOX, were added, and the cells were incubated for different at different time points (15 min, 30 min, 1 h, and 2 h at 37°C, and 30 min at 4°C). 30 min before washing the cells with PBS-BSA 0.1%, the nuclear marker Hoechst (1 μL from a solution 5 mM), and the lysosomal marker Lysotracker Green (10 μL from a solution of 100 μM) were added to identify possible colocalization and therefore establish an endocytic pathway. Finally, cells were washed with PBS-BSA 0.1%. Then, the glass was removed and placed on the microscope chamber with fresh media containing 2 μM of CA-074 inhibitor. Samples were analyzed under the microscope. Images were captured with an inverted DM IRE2 microscope equipped with a λ-blue 60 x oil immersion objective and handled with a TCS SP2 system, equipped with an acoustic optical beam splitter (AOBS). Excitation was performed with an argon laser (Lysotracker Green 496 nm), an HeNe laser (DOX 561 nm), and a blue diode (Hoechst 405 nm). Images were captured at an 8-bit greyscale and processed with LCS software (version 2.5.1347a, Leica Germany) containing multicolor, macro, and 3D components. Control cells that followed the same incubation time were also analyzed to establish the autofluorescence, as well as cells treated only with Hoechst or Lysotracker Green.

Annexin V by Flow Cytometry. 4T1 cells were seeded in 6-well plates at a density of 5,900 cell/cm^2 (1mL cell suspension per well) and allowed to adhere for 24 h. Compounds (sterilized under UV-light) were then added at their calculated IC50 value. After 72 h of incubation, the media was removed and stored. Plates were washed twice with sterile PBS and incubated with 100 μL of trypsin for 5 minutes. After that time, the trypsin was inactivated with previously collected media, and the cell suspension was centrifuged at 400g for 7 minutes. The pellet was then resuspended in Annexin V buffer, transferred to

flow cytometry tubes, and incubated with 5 μL of commercial Annexin V-FITC for 20 minutes. Samples without Annexin V staining were used to determine autofluorescence, whereas untreated samples were used as controls. Samples were then analyzed using a Becton Dickinson FACS Calibur cytometer (California, USA) equipped with an argon laser (488 nm) and emission filter for 550 nm. Data collection involved 10,000 counts per sample, and data were analyzed using CELLQuestTM version 3.3 software.

Cell Cycle by Flow Cytometry. 4T1 cells were seeded in 6-well plates at a density of 5,900 cell/cm^2 (1mL cell suspension per well) and allowed to adhere for 24h. Compounds (sterilized under UV-light) were then added at their calculated IC50 value. After 72 h of incubation, the media was removed and centrifuged at 400 g for 7 minutes while the cell monolayer was kept with PBS. The pellet was resuspended in 500 μL of hypotonic buffer containing sodium citrate, triton, RNase, and Propidium Iodide, and incubated for 24 h at 4 ºC. Samples were kept at 4 ºC until they were analyzed. Samples without PI staining were used to determine autofluorescence, whereas untreated samples were used as controls. Samples were analyzed using a Becton Dickinson FACS Calibur cytometer (California, USA) equipped with an argon laser (488 nm) and emission filter for 550 nm. Data collection involved 10,000 counts per sample, and data were analyzed using CELLQuestTM version 3.3 software.

Statistical Analysis. Data from the experiments were analyzed using two-way ANOVA and Bonferroni post hoc. In all cases, we considered differences to be significant when p***<0.001; p**<0.01; p*<0.05; ns: non-significant.

Tumor model. In vivo antitumor activity evaluation of PGA-DOX NG in 4T1 murine orthotopic model. Animal experiments were performed per the European Communities Council Directive (86/609/ECC) guidelines and by Spanish Royal Decree 1201/2005. All the experimental procedures were approved by the Institutional Animal Care and Use Committee and performed by accredited and trained staff. Food and water were provided ad-libitum during the whole experiments in all cases, and the general aspect, behavior, and body weight were evaluated daily from the beginning of the experiment to ensure

animal welfare. 6-8-week-old female BALB/c mice used for all experimental procedures were purchased from Envigo Laboratories Inc. (Spain, EU). 4T1 tumors were induced by the intradermal injection of 5 x 10^5 4T1 cells suspended in 100 μl of Matrigel (Extracellular Matrix gel 354234 BD at 20% diluted in RPMI media +10% inactivated serum) in the second left mammary fat pad under inhalatory anesthesia (2.5% sevoflurane in 100% oxygen) [3]. Tumors were morphometrically evaluated daily with an electronic caliper, and tumor volumes were obtained by considering tumor shape as spheroids[4]. Eight days after tumor implantation, when the tumor size reached 0.1 cm^3, mice were split into representative groups. Treatments were dissolved in PBS and immediately injected intravenously (i.v.) with three single doses of 10 mg/Kg Dox equivalents in the case of the NGs every three days. Free Dox dissolved in saline was administered at 5 mg/kg as free drug control, following the same schedule. Tumors were measured with a caliper, and volumes were obtained considering them to be spheroids. Once tumors reached 1.0 cm^3 or 16 days after the first treatment, mice were sacrificed under CO^2 atmosphere and blood, and tumors and major organs were collected for molecular analysis. Treatment safety was evaluated by tracking body weight and comparisons with control and healthy animals. The mice under study were examined daily in the search for any pain-related behavior or conduct modification.

Anti-metastatic activity in the Lung and axillary lymph nodes. Lung metastasis was evaluated following a previously described protocol[5] with several improvements described in Arroyo-Crespo et al..[3] Lungs were removed immediately after animal sacrifice and washed in PBS. Tissues were then transferred to a 6-well plate previously filled with 3 ml of cold Hank's Balanced Salt Solution 1X (HBSS - Gibco) and washed twice. Over a new empty 6-well plate, organs were mixed with surgical scissors for 2 min, and 2.5 ml of cold collagenase Type IV (Gibco 17104-019) was added to each well. The tissue mixture was transferred into a 15 ml falcon tube and incubated at 4°C for 90 min in a rotatory shaker at maximum speed. Once the digestion was finished, the largest tissue pieces were broken down, and the final mixture was filtered by gravity through a 70 μm nylon filter (Fisher). The filtered suspension was collected by

adding 5 ml of HBSS 1X in the falcon and then centrifuged at 1,500 rpm (10°C, 5 min). The supernatant was removed, and the pellet was washed twice with 10 ml of HBSS, and the pellet was then suspended in 10 ml of medium (RPMI1640 + 10% FBS + penicillin/streptomycin + fungizone) and seeded in six-well plates (1.4 ml each). The cells were incubated at 37ºC under 5% CO_2, allowing for consistent growth. After five days, every well was washed three times with PBS. 6-thioguanine resistant-cells adhered to the plate, and other cells could be easily removed. 2 ml of fresh medium and 2 μl of 6-thioguanine were added back, and the incubation was allowed to continue. Eleven days after seeding, cells were washed twice with PBS, trypsinized (700 μl of trypsin), and resuspended in 800 μl of the medium. Finally, cells were counted with trypan blue or crystal violet in a dilution according to the degree of confluency.

Western Blot. Western blot analysis was performed to evaluate essential protein from treated tumors after 16 days of treatment in the 4T1 model. Tumors were homogenized in a mortar with liquid nitrogen and proteins extracted using a Protein extraction kit from Millipore Corporation following the manufacturer's instructions. Protein content was determined by Bradford assay. 100 μg protein was then mixed with 5x SDS sample buffer, boiled for 7 min at 95°C to denaturize the protein, and separated through 8% SDS-PAGE gels. After electrophoresis, the proteins were transferred to PVDF membranes (Amersham Pharmacia Biotech, UK) by electrophoretic transfer. The membranes were blocked in 5% skim milk for 2 h, rinsed, and incubated overnight at 4ºC with the following primary antibodies: TF (1:1000) and VEGF (1:1000) from Santa Cruz Biotechnology Inc. and β-actin (1:10,000) from Sigma Aldrich. Excess antibody was then removed by washing the membrane in PBS/0.1% Tween 20, and the membranes were incubated for 1 h with horseradish peroxidase-conjugated secondary antibodies: goat anti-mouse IgG or donkey anti-rabbit IgG (1:5,000) (Santa Cruz Biotechnology Inc., Santa Cruz, CA, USA). After washes in PBS/0.1% Tween 20, immunodetection was performed with the use of the ECL Western blotting detection system (Amersham Pharmacia Biotech, UK), according to the manufacturer's

instructions. Relative protein levels were quantified by densitometry with ImageJ software. Results were standardized using β-actin expression as the reference.

Statistical Analysis. Data from the experiments were analyzed using two-way ANOVA and Bonferroni post hoc. In all cases, we considered differences to be significant when $p^{***} < 0.001$; $p^{**} < 0.01$; $p^{*} < 0.05$; ns: non-significant.

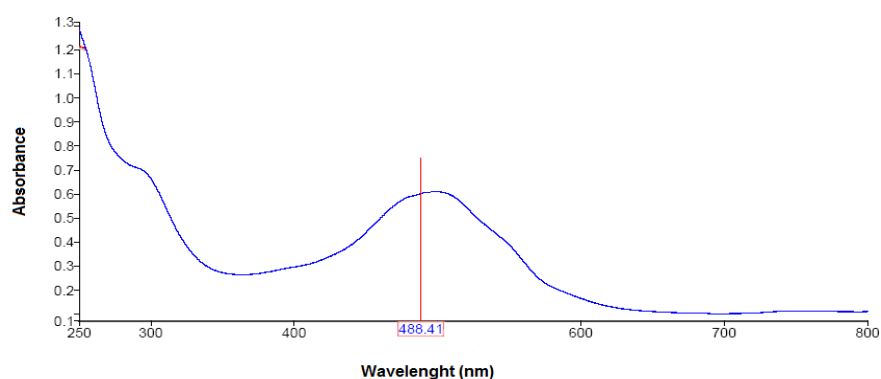## 4. Additional Supporting Figures

4.1. Physicochemical Characterization

Figure S4. UV-Vis spectra of PGA-DOX NGs showing DOX absorbance at 488 nm in H_2O
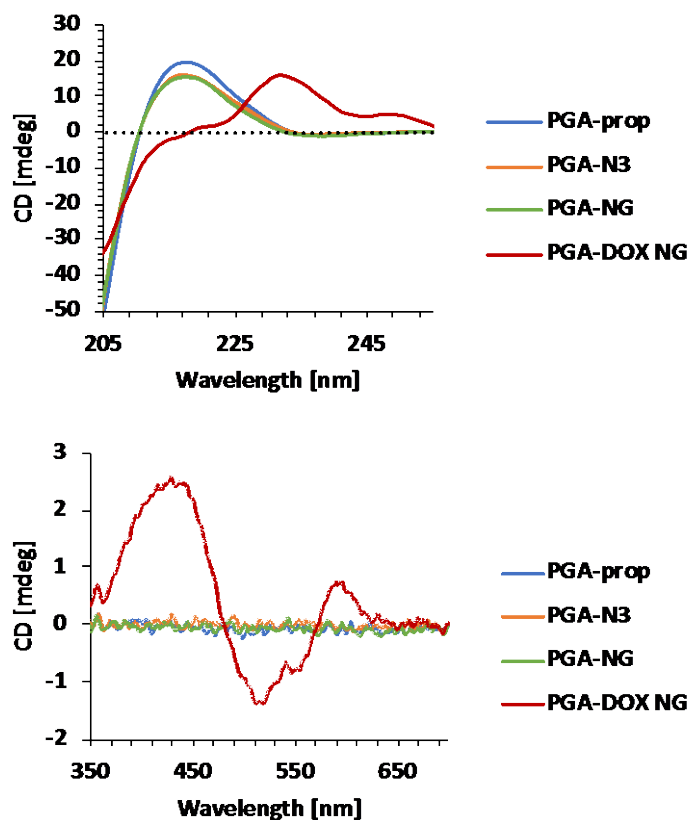
Figure S5. Comparison of CD spectra of PGA precursors, PGA NGs (green), and PGA-DOX NGs (red). Both the regions from 205 to 255 nm (A) and from 350 to 700 nm (B) show the influence of DOX in the random coil secondary structure of the gel. The CD spectrum of PGA-DOX NGs shows the typical peaks of the DOX chromophore with its set of $\pi \rightarrow \pi^*$ and $n \rightarrow \pi^*$ transitions, and the characteristic negative band at 540 nm for DOX dimerization[7].
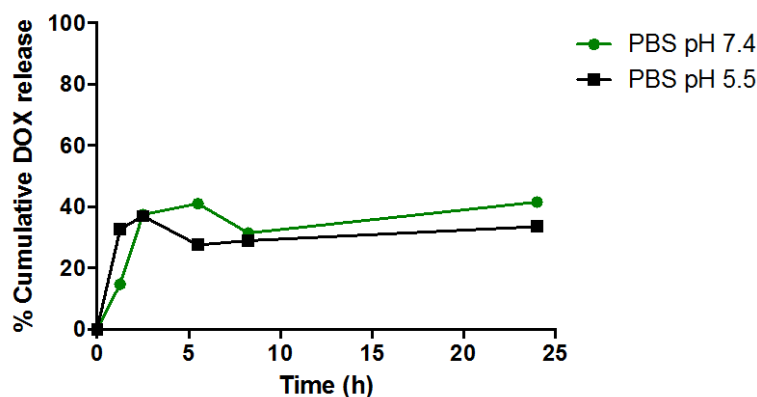

Figure S6. Drug release profile of PGA-DOX NG at different pH control conditions (pH 5.5, squares, pH 7.4, circles) at different time points (n=3, data as mean ± SEM).
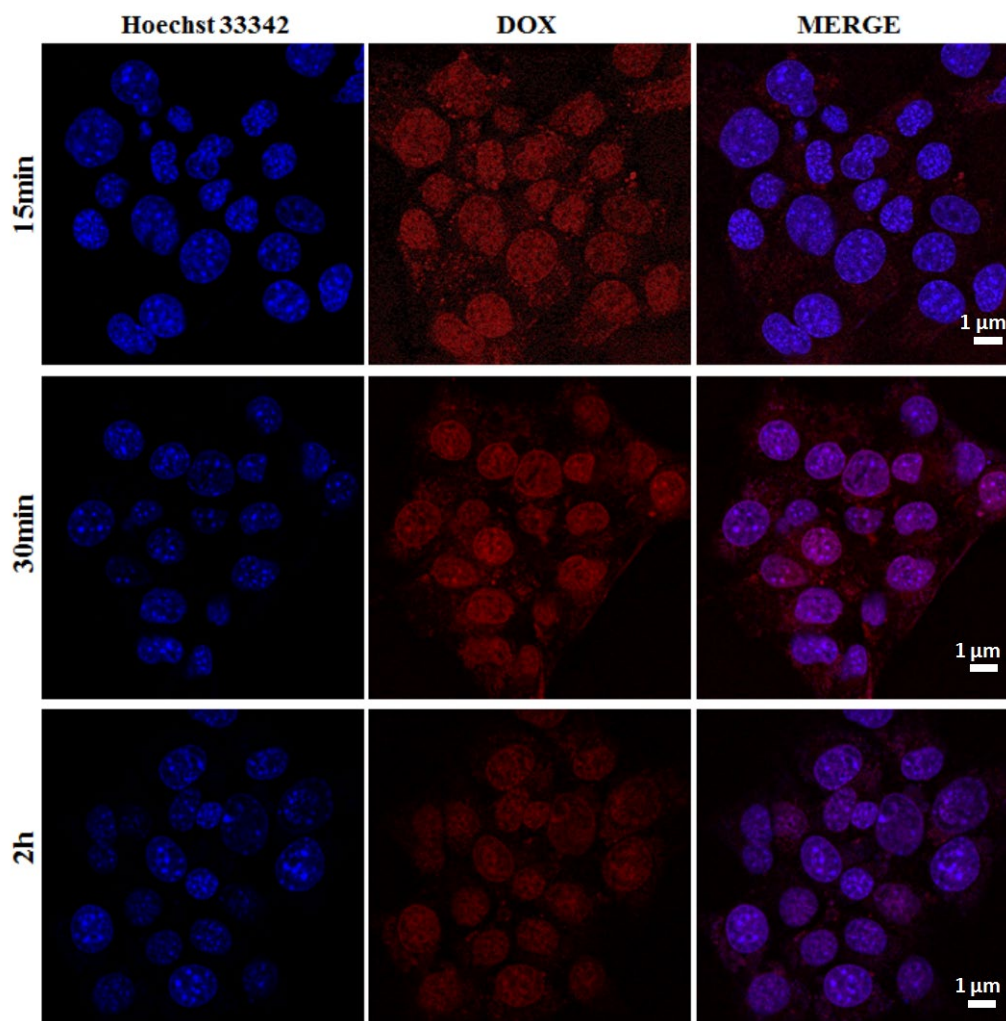
4.2. Cell-based Assays

Figure S7. Confocal images of Dox cellular uptake in 4T1 cells at different time points a pulse-chase experiment (Blue-Hoechst 33342 for nuclei; Red-Dox associated fluorescence).
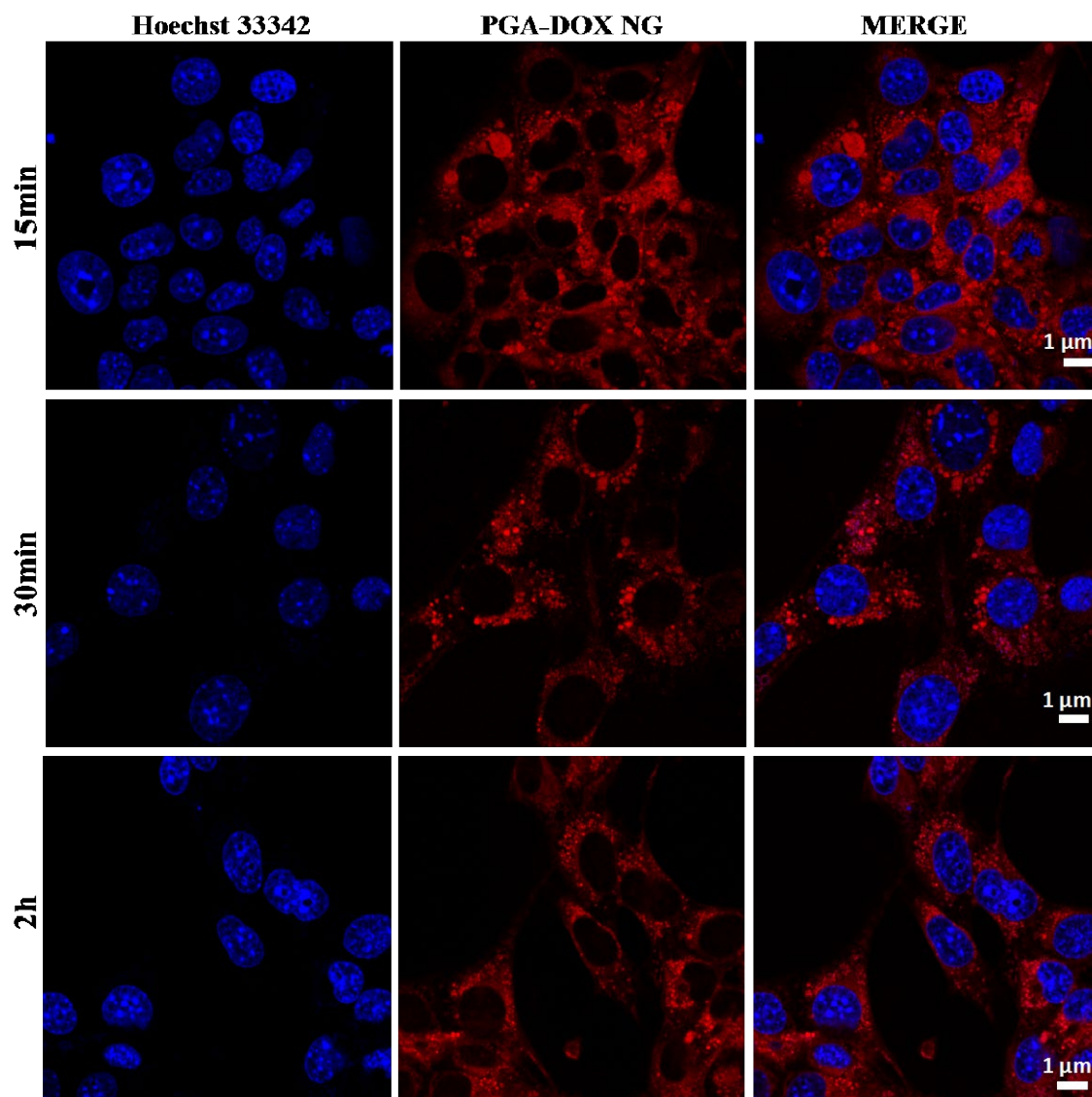
Figure S8. Confocal images of PGA-Dox NG cellular uptake in 4T1 cells at different time points a pulse-chase experiment (Blue-Hoechst 33342 for nuclei; Red-Dox associated fluorescence).
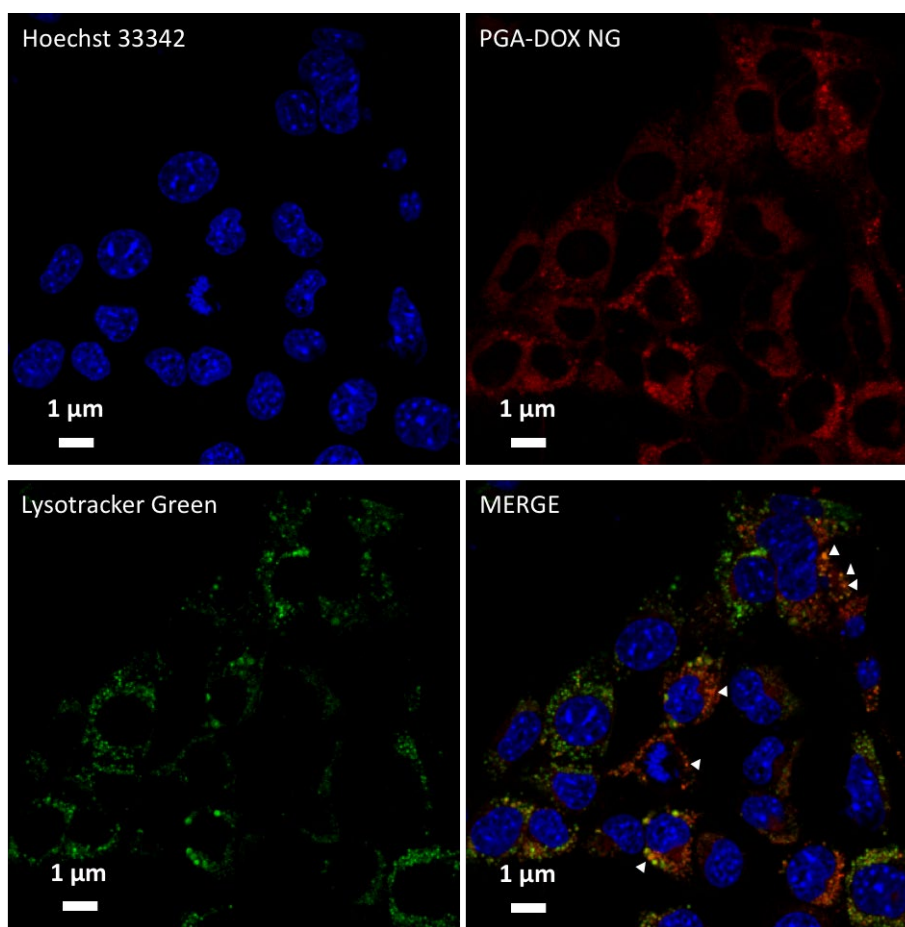
Figure S9. Confocal images of PGA-Dox NG uptake at 1h post-treatment in 4T1 cells following a pulse-chase experiment (Blue-Hoechst 33342 for nuclei; Red-Dox associated fluorescence, Green-LysoTracker Green). Colocalization with the LysoTracker marker was observed (merged in yellow). White triangles highlight representative colocalization.

Table S2. IC50 values of free DOX and PGA-DOX NG in 4T1 cells, 72 h of treatment, as determined using GraphPad Prism 5 using non-linear regression to fit the data of the MTS assays to the log(inhibitor) vs. response (variable slope).

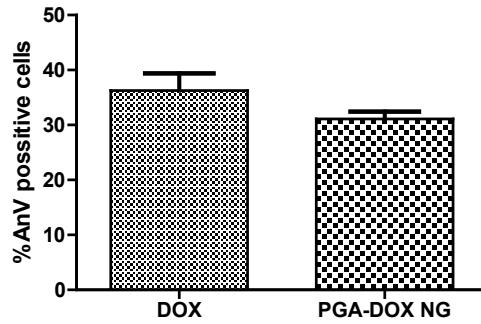| Compound	IC50 (µg/mL eq. DOX)
Free DOX	0.1824
PGA-DOX NG	0.3102

Figure S10. % Annexin V positive cells after 72h of incubation, as measured by flow cytometry using Dox and PGA-Dox NGs at the IC50 obtained for MTS assays. Results are the mean ± SEM of three independent experiments with two replicates each. A *t*-test was used for comparison between groups. The results were not statistically significant.
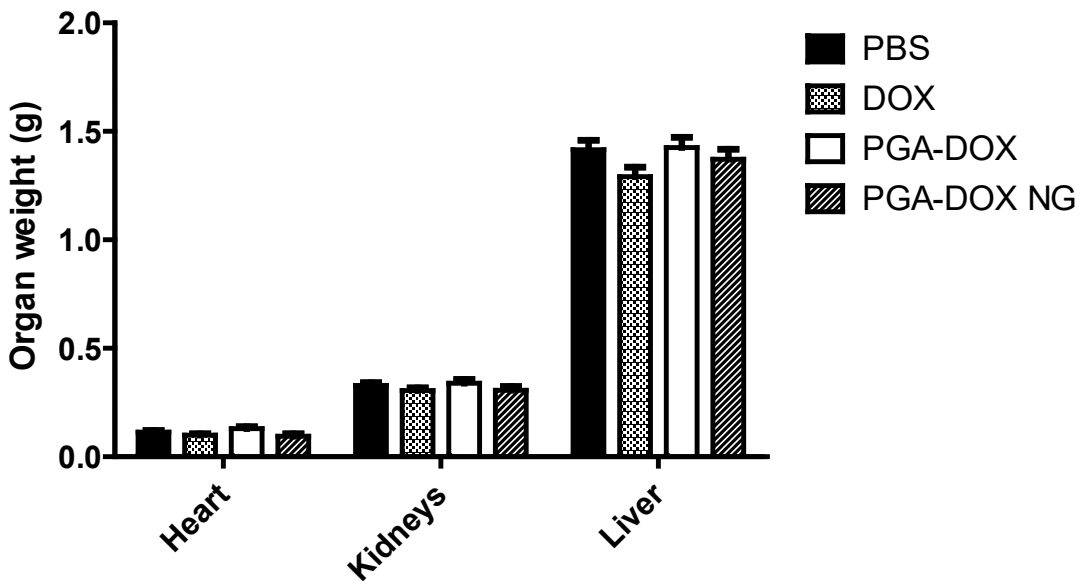
4.3. *In vivo* Data

Figure S11. Weight of critical organs (heart, kidney, and liver) from orthotopic 4T1 breast tumor mice after sacrifice at day 15. Non-significant differences were found after one-way ANOVA and Bonferroni post hoc, used for comparison between groups.

References

1.   Barz, M.; Duro-Castano, A.; Vicent, M. J., A versatile post-polymerization modification method for polyglutamic acid: Synthesis of orthogonal reactive polyglutamates and their use in "click chemistry." *Polymer Chemistry* **2013,** *4* (10), 2989-2994.

2.   Sousa-Herves, A.; Espinel, C. S.; Fahmi, A.; González-Fernández, Á.; Fernandez-Megia, E., In situ nanofabrication of hybrid PEG-dendritic–inorganic nanoparticles and preliminary evaluation of their biocompatibility. *Nanoscale* **2015,** *7* (9), 3933-3940.

3.   Arroyo-Crespo, J. J.; Armiñán, A.; Charbonnier, D.; Balzano-Nogueira, L.; Huertas-López, F.; Martí, C.; Tarazona, S.; Forteza, J.; Conesa, A.; Vicent, M. J., Tumor microenvironment-targeted poly-L-glutamic acid-based combination conjugate for enhanced triple negative breast cancer treatment. *Biomaterials* **2018,** *186*, 8-21.

4.   Arroyo-Crespo, J. J.; Armiñan, A.; Charbonnier, D.; Forteza, J.; Palomino-Schatzlein, M.; Pineda-Lucena, A.; Vicent, M. J., Triple-negative Breast Cancer Preclinical Models Provide Functional Evidence of Metastatic Progression and Suitability for Nanomedicine Evaluation *Cancer Research* **2018,** *Under Review*.

5.   Arroyo-Crespo, J. J.; Deladriere, C.; Nebot, V. J.; Charbonnier, D.; Masiá, E.; Paul, A.; James, C.; Armiñán, A.; Vicent, M. J., Anticancer Activity Driven by Drug Linker Modification in a Polyglutamic Acid-Based Combination-Drug Conjugate. *Advanced Functional Materials* **2018,** *28* (22), 1800931.

6.   Pulaski, B. A.; Ostrand-Rosenberg, S., Mouse 4T1 breast tumor model. *Current protocols in immunology* **2001,** *Chapter 20*, Unit 20 2.

7.   Gallois, L.; Fiallo, M. Garnier-Suillerot, A. Comparison of the interaction of doxorubicin, daunorubicin, idarubicin and idarubicinol with large unilamellar vesicles: Circular dichroism study. *Biochimica et Biophysica Acta (BBA) – Biomembranes* **1998,** 1370 (1), 31-40